Electrical Transport properties of amorphous $Ge_{15}Te_{85}$ thin films using scanning probe microscopy for phase change memory applications

Myana Santoshkumar

A Dissertation Submitted to

Indian Institute of Technology Hyderabad

In Partial Fulfillment of the Requirements for

The Degree of Master of Technology

भारतीय प्रौद्योगिकी संस्थान हैदराबाद

Indian Institute of Technology Hyderabad

Department of Materials Science and Engineering

July, 2013

Declaration

I declare that this written submission represents my ideas in my own words, and where others' ideas or words have been included, I have adequately cited and referenced the original sources. I also declare that I have adhered to all principles of academic honesty and integrity and have not misrepresented or fabricated or falsified any idea/data/fact/source in my submission. I understand that any violation of the above will be a cause for disciplinary action by the Institute and can also evoke penal action from the sources that have thus not been properly cited, or from whom proper permission has not been taken when needed.

(Signature)

Myana Santoshkumar

MS11M05

Approval Sheet

This thesis entitled **"Electrical Transport properties of amorphous $Ge_{15}Te_{85}$ thin films using scanning probe microscopy for phase change memory applications"** by **Myana Santoshkumar** is approved for the degree of Master of Technology from IIT Hyderabad.

Dr. Suhash Ranjan Dey
Department of Materials Science and Engineering
Examiner

Dr. M. Deepa
Department of Chemistry
Examiner

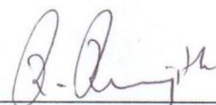

Dr. Ranjith Ramadurai
Department of Materials Science and Engineering
Adviser

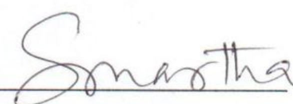

Surendra Kumar Martha
Department of Chemistry
Chairman

Acknowledgements

I express my sincere thanks to **Dr. Ranjith Ramadurai**, who was very much encouraging, patient to make me understand the things and helpful for his timely suggestions during the odds. Indeed, I am privileged to have you as my teacher and my project supervisor.

I would like to thank **Dr. M. Anbarasu**, assistant professor in the Department of Electrical Engineering, IIT Indore for providing me the samples, helping with the valuable discussions and most importantly for being the reason for my M.Tech project.

I want to thank all my faculty **Dr. Pinaki Prasad Bhattacharjee**, **Dr. Suhash Ranjan Dey**, **Dr. Atul Suresh Deshpande** and **Dr. Bharat Bhooshan Panigrahi** for their valuable teaching during my course work.

I want to thank **Kumaraswami miriyala** Ph.D scholar for his co-operation during my experimental work. I also express my gratitude to **Mallesham Bandi** and **Venkateshwarrao Mannepalli** for their help during the experimental work and their support in all kinds during my stay at IITH.

I would like to thank all the Ph.D scholars, my classmates and other M.Tech colleagues of Department of Materials Science and Engineering for their help, support and for the most memorable moments.

Lastly, I would like to thank all my friends at IITH for providing all I wanted and making my stay at IITH a memorable.

Dedicated to

My Family and my friends…

Abstract

Chalcogenide glassy semiconductors exhibit ultrafast reversible electrical switching from highly resistive 'OFF' state to a low resistive 'ON' state in the amorphous phase under the excitation of suitable electrical pulses. The contrasting features associated with the amorphous and crystalline phases are exploited for use in phase change memory (PCM) devices. The phase change memories are considered as potential candidates to replace the conventional flash memories due to their low energy consumption and scalability. Phase change materials are characterized by their programming characteristics, such as programming currents and programming speeds. Faster crystallizing materials such as GeTe and $Ge_2Sb_2Te_5$ have proven to be potential candidates for phase change memory. In spite of the slow crystallization exhibited by $GeTe_6$ it shows a stable switching and is used as ovonic threshold switching (OTS) selector device in a memory device. The dual stage crystallization of $GeTe_6$ is the major drawback which has to be analyzed for fabricating OTS device which is better compatible with a phase change memory cell.

In this study, $GeTe_6$ amorphous thin films were fabricated by dc-magnetron sputtering on silica substrates. The amorphous nature and the composition of the fabricated $GeTe_6$ sputtered thin films were studied using x-ray powder diffractometer and SEM-EDS studies respectively. Raman scattering studies were done to understand the local atomic environment present in the amorphous phase of $GeTe_6$.The morphological and electrical properties of thin films were studied using an atomic force microscopy (AFM, Multimode8, make: Bruker) operating in conductive mode(C-AFM). The roughness of thin films is observed in a range from 1.5 nm to 2 nm which substantiates that the thin films are so smooth. Threshold switching and memory switching behavior of thin films with the application of different biasing voltages were analyzed. The possibility of nanoscale control on the memory state of the thin films utilizing C-AFM was studied. The studies unambiguously confirm the possibility of control over the memory state at nanoscale in $GeTe_6$ like thin films.

Nomenclature

PCM – Phase change memory

PCRAM – Phase change random access memory

EXAFS – Extended X-ray absorption fine spectrum

OTS – Ovonic threshold switching

DUT – Device under test

C-AFM – Conductive atomic force microscopy

SEM – Scanning electron microscopy

EDS – Energy dispersive X-ray spectroscopy

Si(Li) – Lithium drifted Silicon

STM – Scanning tunneling microscope

PSPD – Position sensitive photo detector

HOPG – Highly oriented pyrolytic graphite

Contents

Declaration.......ii

Approval Sheet.......iii

Acknowledgements.......iv

Abstract.......vi

Nomenclature vii

1 Introduction....... 10 - 19

1.1 Motivation and Evolution of phase change memory.......10

1.2 Phase change materials.......12

1.3 Principle of phase change recording.......13

1.4 Application need of a phase change memory.......15

1.5 Applications of phase change memory materials.......16

2 Literature Review .... 20 - 30

2.1 Amorphous semiconductors.......20

2.1.1 Introduction.......20

2.1.2 Electrical conduction in amorphous semiconductors.......22

2.2 Chalcogenide semiconductors for phase change memory.......23

2.3 Ge-Te system.......24

2.2.1 GeTe as a phase change memory material.......25

2.2.2 $Ge_{15}Te_{85}$ 26

2.4 Motivation to the present work.......29

2.5 Objectives of the present work.......29

3 Experimental Details .... 31 - 54

3.1 Scanning Electron Microscopy.......31

3.1.1 Energy Dispersive X-ray Spectroscopy (EDS).......34

3.2 X-ray Diffraction.......36

3.2.1 Bragg's Law.......36

3.2.2 X-ray diffractometer.......39

3.3 Raman Spectroscopy.......40

3.3.1 Raman spectrometer.......42

3.4 Atomic Force micoscopy.......43

3.4.1. History.......43

3.4.2. Introduction and principle of operation……………………………………………..44
3.4.3. Basic instrumentation of AFM…………………………………………………45
3.4.4.Modes of operations…………………………………………………………….48
3.4.5.Conductive atomic force microscopy…………………………………………...50
3.4.6.Laboratory Instrument…………………………………………………………..51

4 Results and Discussions .... 55 - 78
4.1 Compositional analysis by Energy dispersive x-ray spectroscopy (EDS)………...55
4.2 Structural characterization of $Ge_{15}Te_{85}$ thin films by XRD……………………….56
4.3 Raman spectroscopy studies of $Ge_{15}Te_{85}$ thin films………………………………57
4.4 Conductive force microscopy studies of standard specimen- Highly oriented pyrolytic graphite (HOPG)…………………………………………………………58
4.5 Electrical characterization of amorphous $Ge_{15}Te_{85}$ thin films……………………..66
4.5.1. Morphology of amorphous thin films…………………………………………..66
4.5.2. I-V characteristics of amorphous thin films……………………………………69
4.5.4. Memory switching of amorphous thin films…………………………………...73
4.5.5. Delay time dependence on switching behavior of amorphous thin films………76

5 Summary and Conclusions .... 79 - 81

Chapter – 1

Introduction

1.1 Motivation and Evolution of phase change memory

In the modern world, the advent of computers is a critical genre that greatly distinguished the invention of pen and paper and other sources to store and manipulate the information. The invention of semiconductor technology has been the key to many other inventions of memory gadgets compiling their efficiency and reliability. The assessment of memory technology went on to achieve the programming speeds, data manipulation, retention, endurance and scalability demanded. As Moore's law stated, the number of memory cells embedded per square inch of chip area would double every year [1]. Thus following Moore's law, the semiconductor industry has made numerous efforts to scale down the size of the devices.

Though numerous efforts has been made to integrate large density of devices in a given area, one of the major drawback was large power dissipation during the operation. Power dissipations can strongly influence the stability and the overall performance of the system. Keeping in mind the power losses during the operation of a system, there has been continuous drive in search of materials that perform at lower operating voltages. Phase change materials possess unique characteristics, by exhibiting reversible phase transformation between amorphous to crystalline and vice versa at the expense of low energy. Hence, memory devices utilizing phase change materials were believed to serve the industry with low power dissipation. Phase change memory (PCM) is a novel technology, which offers down scaling features in accordance with Moore's law. PCM technology is very much successful in rewritable optical data storage media and also regarded as an efficient non-volatile electronic memory, providing high speed memory switching and considered being the potential replacement for conventional flash memories [2].

The investigations on PCM were initiated on Chalcogenide based semiconductor alloys in late 1960s. Though S.R.Ovshinsky is credited as the inventor of phase change materials, the first explanation on phase change materials and memory devices was patented by a group (Dewald, Northover and Pearson) of Bell telephone laboratories [1]. They explained the devices made with As-Te-I alloys that exhibited a negative differential resistance which is a prominent attribute for threshold switching in phase change materials [1]. Their work was patented in 1966 on "Multiple resistance semiconductor elements" [1]. Later Ovshinsky also submitted a series of his findings of resistance switching or current controlled devices and materials and got patented in 1966 [1]. He demonstrated the operation of a PCM cell composed of 48 at. % tellurium, 30 at. % arsenic, 12 at. % silicon and 10 at. % germanium, which required 10 μs to crystallize [3]. Compared to Dewald et.al patent, the claims in Ovshinsky's patent covered broad possible device configurations and operations. By 1970, the company R. G. Neale and D. L. Nelson of Energy Conversion Devices published their results in collaboration with Intel's Gordon Moore which featured the world's first phase change memory device, a 256 bit memory array comprised of 16×16 matrix [1]. The memory cells with 10μm geometry took 5 μs, 200 mA at 25 V bias for the reset operation and 10 ms, 5 mA at 25 V bias for the set operation. Due to high power consumptions and the large volume of phase change material needed to be switched and comparably low performance with the contemporary electrical programmable read only memory (PROMs) of the same period, such a PCM device was not commercialized. Though the PCM technology is a self-made technology in optical data storage applications, lot of research is going on in electronic memory applications to achieve scalable device with power efficiency.

PCM technology is a state of art technique for optical data storage applications. Feinleib et al. were the first to report the laser induced crystallization and its reversibility in amorphous chalcogenide semiconducting films of $Te_{81}Ge_{15}Sb_2S_2$ [1, 4]. They found that the phase change from amorphous to crystalline with the application of laser beam will be accompanied by the change in the reflectivity because of the shift in the absorption edge to lower energy [4]. But the crystallization times were observed to be of the order of microseconds, which was considered unsuitable for any technological applications that require high performance speed. After few years, the research in phase change memory in optical storage media was advanced with the discovery of fast switching materials by Yamada et al. [1]. They revealed that most of the fast switching materials were discovered

on the pseudo binary line between GeTe and Sb_2Te_3 in the ternary diagram of Ge-Sb-Te. Their findings in the publication reported the faster crystallization of $GeSb_2Te_4$ stoichiometric composition of 50ns with static laser irradiation [1].

The data storage density in optical storage media enormously increased from 650 MB (CD-RW) to few hundreds of giga bytes in Blue-ray Discs (BD) with multiple layers, with each layer accommodating up to 25 GB [2]. With the invention of electric field induced and laser irradiated crystallization in chalcogenide based amorphous semiconductors, enormous research was carried out to find the optimized phase change materials which can meet the demands of phase change memory applications.

1.2 Phase change materials

Phase change materials have a potential to reversibly switch between amorphous and crystalline phase under the application of electric fields or laser irradiations. The characteristic property of phase change materials that associated with the phase change is their high contrast in electrical resistivity or optical reflectivity between both of the phases [5, 6]. Such eminent property was first observed in amorphous chalcogenide (group VI of the periodic table) alloys, which are good glass formers. These glasses predominantly form two fold- coordinated covalent bonds which form linear tangled and polymer like clusters in their melt state, which on further prevents the atomic motion necessary for crystallization [7]. GeTe and $Ge_2Sb_2Te_5$ are the widely studied chalcogenide semiconductor materials employed in phase change memory applications.

The most interesting phenomenon that contributes to the transport characteristics in glassy chalcogenide semiconductor materials is threshold switching. At threshold switching the chalcogenide semiconductor exhibits a change in resistive state, which forms the basic need of a two state device. Threshold switching mechanism in phase change materials was first reported by Ovshinsky [3] in the late 1960s. Subjecting the phase change material to a switching delay at threshold voltage results in joule's heating due to the increment of current, which effectively leads to a transformation to crystalline phase. This transition to the crystalline phase is commonly associated with a negative differential resistance behavior after threshold switching. The instability that brings the most intriguing property of negative differential resistance is not well understood. Generally, threshold switching results in a transition from amorphous to crystalline. Such a switching is called memory switching. But, few materials will not undergo any phase change except the

resistive change, since they have high crystallization temperatures. This transition from the amorphous to crystalline phase depends on the joule heating resulting from the large current and is possible for the materials with low crystallization points [1]. Threshold switching is always discerned from memory switching, as it does not involve any structural transformation and it is more particular to amorphous phase, i.e. resistive switching in amorphous phase [8]. Numerous research work is being carried out on understanding the phenomenon of threshold switching and determine whether the effect is thermal or electronic.

1.3 Principle of phase change recording:

PCMs manipulate the large contrast in the optical or electrical property between the amorphous and crystalline states to store the information.

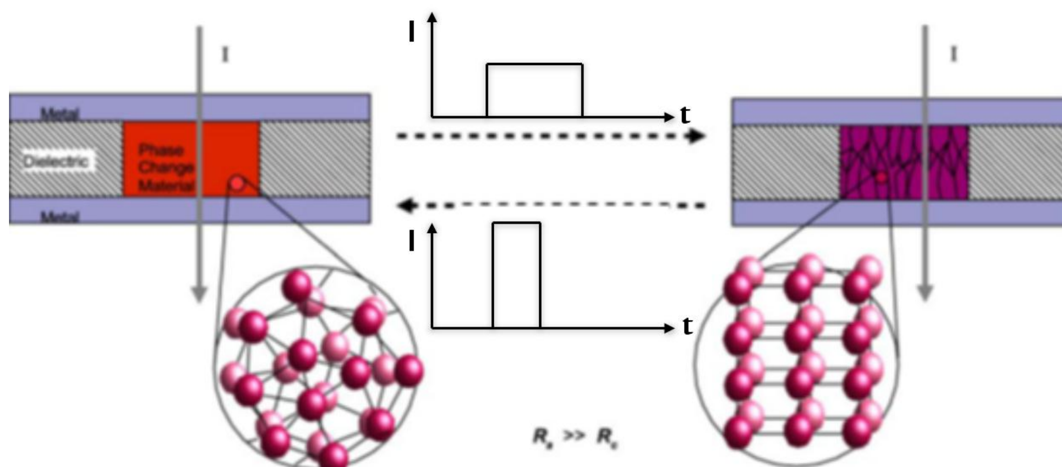

Fig 1.3.1: Electrical switching of PC materials for non-volatile electronic storage. A current pulse of high intensity and short duration (bottom) is used for amorphization, while a pulse of lower intensity but longer duration (top) re-crystallizes the material. Read-out is performed at lower currents that do not change the state of a bit. Image reproduced from [9]

Figure 1.3.1 demonstrates the operation of a phase change memory device with the application of electrical pulses. In a phase change memory device, a small phase change material undergoes a phase transition between amorphous to crystalline provided with sufficient electrical pulses or laser pulses. To write the data in a PCM device, a narrow pulse is given to phase change material which heats up the material to its melting point. Sudden quenching from a melt state bypasses the crystallization and the material becomes amorphous. This is called 'reset' operation. Now to erase the information, sufficiently

broad pulse is applied which can heat up the material above to its glass transition temperature (T_g). The longer stay above T_g clears the tangled bonds in the amorphous state and makes the material crystalline. This is called 'set' operation [10]. Now to read the information from the PCM device, a low intensity pulse is applied to determine the electrical resistance or optical reflectivity of the device. Always, a read pulse is applied which will not disturb the state of the device [1, 10].

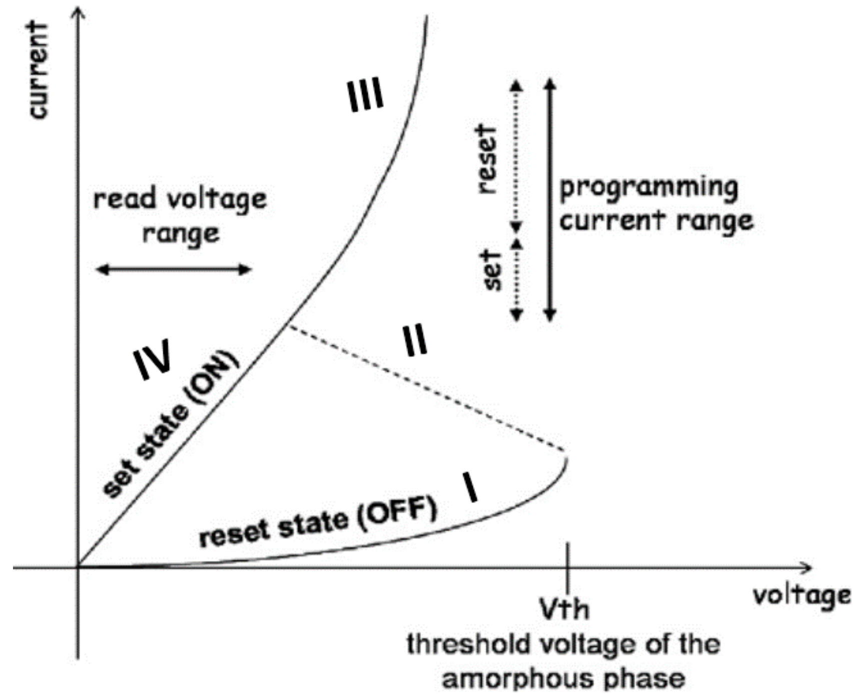

Fig 1.3.2: A typical I-V characteristics of a phase change memory device. Image reproduced from reference [11]

The current-voltage characteristics shown in figure 1.3.2 has four major sections. Region I represents that there is no appreciable current in the high resistive amorphous state, but when the voltage exceeds a threshold value, there is a possible joule heating effect which turns the amorphous state to a highly conductive state shown by the voltage snap back (region II) shown in the figure. The snap back effect can be seen till the holding voltage. The holding voltage is the voltage where we can observe a transformation from low resistive state to high resistive state in the amorphous material when decreasing the voltage below the threshold switching value. The current when further increases as a result of joule heating with the application of voltage, the material gets transformed to crystalline phase which is a high conductive state (Region III). This is called SET operation for the device. Since, we have understood that crystalline chalcogenide semiconductors are highly

conductive, they exhibit a linear I-V characteristics even with decreasing the voltage unto a possible zero voltage by being stable in their crystalline phase (Region IV). The read voltage applied to measure the state of the device is always lower than the threshold switching voltage of the device [1].

1.4 Application need of a PCM

A phase change material, should undergo a phase transformation from amorphous to crystalline state with applied electric pulses or laser irradiatoins as explained earlier. Hence, it has to possess both stable amorphous and crystalline state for many years at operating temperatures. The resistivity contrast between both the amorphous and crystalline states should be at least more than three orders of magnitude at operating temperatures to differentiate them electrically. The operating temperatures should be as high as the device characteristics can't be tolerated with the temperatures. The crystallization times should be of several tens of nano seconds at operating temperatures and it should not vary with device operation for many years. The material should switch repeatedly between the states for many cycle comparable with the flash memories. The crystallization temperatures should be greater than the temperature and this should not be decreased with the increasing number of cycles. The melting temperatures for the material should be as low as possible so that the programming currents will be low to achieve the amorphization. There should not be any chemical reaction i.e., change in chemical composition by phase seperation, reaction with the contact material and it should not happen with the melt quenching and crystallization operations. The device characteristics should not be affected by several(10^5) repetitive cycles. The failure temperatures for the device should be as high as possible and should be consistent for several years. The repetitive cycles should not lead to any kind of device failures such as phase seperation of materials, void formation and delamination. The scaling properties of materials is of high importance for device fabrication [12]. To make an ideal phase change memory device is challenging with having fulfilled the aforementioned requirements.

1.5 Applications of phase change materials

By exploiting the property of phase change associated with the resistivity or reflectivity contrast between the phases, phase change materials are employed in electronic and optical data store media.

[a]. Optical data storage:

Typically optical data storage depends on the contrast in reflectivity of amorphous and crystalline phases when they are read. The data storage operation is mainly governed by writing and erasing speeds and reading is always much faster. The writing (amorphization) is attained by applying laser pulses of particular wave length for a very short time, which induces the joule heating and melts the material which is subsequently quenched to form an amorphous phase. The erasing of an amorphous bit is attained by applying laser pulses for relatively longer times which anneal the material above the crystallization temperature to form a crystalline phase. Reading of a bit is acquired by applying low intensity laser pulse which will not disturb the state of the material. Below is the figure shows the typical phase optical disc.

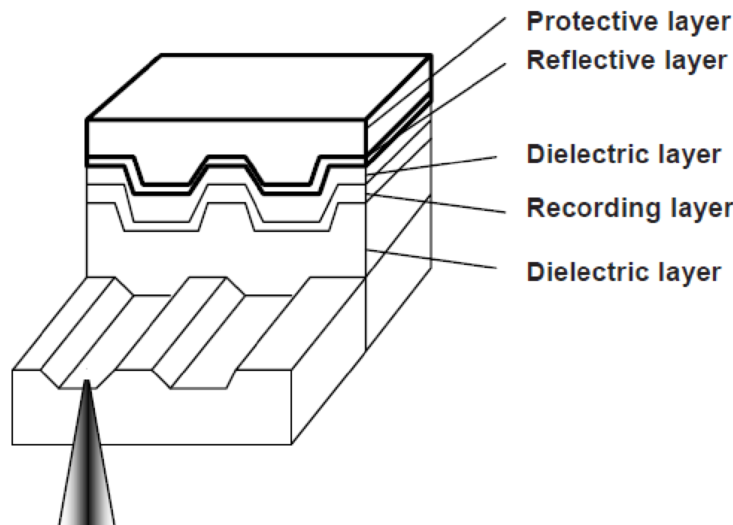

Fig 1.5.1: The structure of a typical phase change optical disc. Image is reproduced from ref [6].

In a typical phase change optical disk, there are four different layers namely, protective layer, reflective layer, recording layer and two dielectric layers. All of the four layers are deposited on a poly carbonate substrate on which it has grooves which directs the laser beam during the operation. All the four layers should have large absorption co-efficient for the wavelength of laser beam. The recording layer or the phase change layer is sandwiched between two dielectric layers made of ZnS-SiO_2. The dielectric layers have

large refractive index to permit the laser beam to best resolution on the recording layer. These also prevent the thermal damage to the poly carbonate substrate while the write, read and erase operations by adjusting the lower dielectric layer to be thick enough to prevent the heat diffusion. The reflective layer provides the mechanical protection to the substrate and also acts as a heat sink by taking the heat from the recording layer to make a rapid quenching effect which leaves the area to amorphous. It also acts as a reflector to attain high sensitivity for measurements [1].

In the optical drives, the optical disc rotates with a specific velocity. The laser beam with a particular power and wave length falls on the grooves of the recording layer with a diameter of few microns. The laser irradiation time is in the order of few tens of nano seconds. To write an amorphous bit, the laser beam with a narrow pulse width falls on the recording layer through the permission of other layers melts the area. The heat is dissipated to the reflective layer through the thin upper dielectric layer in a short time makes a rapid quenching effect. Since the lower dielectric layer is thick enough, it won't damage the substrate thermally which has a low tolerance of heat. To read the bit on the recording layer a laser beam of low intensity is used. Since the amorphous bit absorbs the laser beam, a weak signal reflected to the detector is read. To erase the bit, a laser beam of broad pulse width with relatively high intensity is used which anneal the bit area makes the atoms to rearrange and the area becomes crystalline [1].

Till now, there are three generations of optical storage media developed. The first generation of optical media started with compact disc (CD) with CD-R and CD-RW applications in both audio and video formats with a storage capacity of 650 MB data. Later in the second generation, it extended to digital versatile discs (DVD) with a storage capacity up to 4.7 GB. In the third generation, the data storage capability is increased to a storage of more than 25 GB by employing Blue ray discs (BD). BDs meet the requirements of high defintion (HD) quality data experience in the global availability [1, 2]. The challenges of optical storage media is to be storing the data for tens of years with room temperatue operations.

[b]. Phase change random access memory (PCRAM)

After the success of PCM materials in optical storage media, the research went on to find the development in electronic storage media employing phase change materials. The motivation for the evolution of PCM electronic technology is to overcome the scaling

problems arised with the storage charge non volatile memories. Phase change electronic memory is one among such electronic storage media for achieving the best scaling with a faster device operation. The shematic phase change random access memory cell, so called mushroom cell is given below.

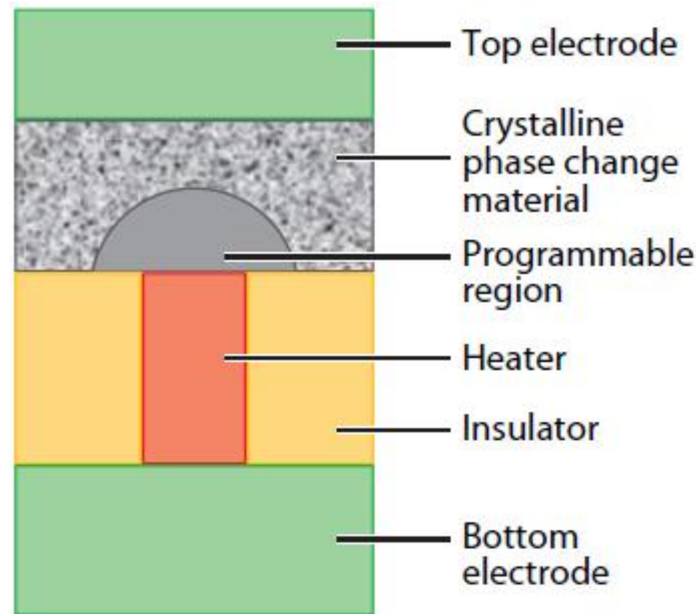

Fig 1.5.2: A schematic of a mushroom PCRAM cell. A typical electrode material is TiN and an insulating materials is SiO_2 and the phase change material is consisting of a doped $Ge_2Sb_2Te_5$. Image is reproduced from ref [12]

To program a bit of PCM cell, a fast and high current pulse is given which makes the programmable region melted and the volume drops and by removing the pulse the region gets amorphous. This is called RESET of the cell. When a longer current pulse of high current is given, it raises the temperature of the region above the crystallization temperature and by giving the sufficient annealing time, the region gets back to crystalline state of low resistance state. This is called SET of the cell. The bit stored in the cell is read by a low current pulse which reads the high resistance state or low resistance state of the cell. PCM cells based on GeTe exhibit good data retention characteristics which endure 1 x 10^5 cycles with a crystallization time of 30 ns. The data retention is stable up to 160 ˚C and the SET/RESET contrast is stable up to three decades [13]. The future applications of PCM include the fabrication of high density data storage memory arrays, embedded memories in logic circuits. It can also be used as a memory cell selector which is better compatible with a phase change memory cell.

References

1. Raoux, Simone. Phase change materials. Springer, 2009.
2. Wuttig, Matthias, and Noboru Yamada. "Phase-change materials for rewriteable data storage." Nature materials 6, no. 11 (2007): 824-832.
3. Ovshinsky, Stanford R. "Reversible electrical switching phenomena in disordered structures." Physical Review Letters 21, no. 20 (1968): 1450-1453.
4. Feinleib, J., J. DeNeufville, S. C. Moss, and S. R. Ovshinsky. "Rapid Reversible Light-Induced Crystallization of Amorphous Semiconductors." Applied Physics Letters 18, no. 6 (1971): 254-257.
5. Raoux, S_, G. W. Burr, M. J. Breitwisch, C. T. Rettner, Y-C. Chen, R. M. Shelby, M. Salinga et al. "Phase-change random access memory: A scalable technology." IBM Journal of Research and Development 52, no. 4.5 (2008): 465-479.
6. Burr, Geoffrey W., Matthew J. Breitwisch, Michele Franceschini, Davide Garetto, Kailash Gopalakrishnan, Bryan Jackson, Bulent Kurdi et al. "Phase change memory technology." Journal of Vacuum Science & Technology B: Microelectronics and Nanometer Structures 28, no. 2 (2010): 223-262.
7. Hudgens, S., and B. Johnson. "Overview of phase-change chalcogenide nonvolatile memory technology." MRS bulletin 29, no. 11 (2004): 829-832.
8. Anbarasu, M., and Matthias Wuttig. "Understanding the Structure and Properties of Phase Change Materials for Data Storage Applications." Journal of the Indian Institute of Science 91, no. 2 (2012): 259-274.
9. Wuttig, M., and C. Steimer. "Phase change materials: From material science to novel storage devices." Applied Physics A 87, no. 3 (2007): 411-417.
10. Lencer, Dominic, Martin Salinga, and Matthias Wuttig. "Design Rules for Phase-Change Materials in Data Storage Applications." Advanced Materials 23, no. 18 (2011): 2030-2058..
11. Sousa, Véronique. "Chalcogenide materials and their application to Non-Volatile Memories." Microelectronic Engineering 88, no. 5 (2011): 807-813.
12. Simone Raoux, “Phase change materials”,Annu. Rev. Mater. Res, 39, 25-48, 2009.
13. Perniola, Luca, Veronique Sousa, Andrea Fantini, Edrisse Arbaoui, Audrey Bastard, Marilyn Armand, Alain Fargeix et al. "Electrical behavior of phase-change memory cells based on GeTe." Electron Device Letters, IEEE 31, no. 5 (2010): 488-490..

Chapter 2

Literature Review

This chapter gives the brief about the phenomenon of phase change mechanism in amorphous chalcogenide semiconductors. We also discuss about the binary GeTe materials that have been employed in phase change memory technology and selector devices.

2.1 Amorphous Semiconductors

2.1.1 Introduction

The surge of interest in amorphous semiconductors came to light with the Ovshinsky's invention of various types switching in amorphous chalcogenide semiconductors [1]. Understanding the physics of various types of switching in amorphous semiconductors is the driving force for the researchers to work on these materials for the last five decades. Amorphous semiconductors laid the foundation for the invention of phase change electrical memory, which became so popular among the other existing memory technologies. Because of the presence of various co-ordination in a given compound of amorphous semiconductor compared to crystalline semiconductor, it was so interesting to investigate the electrical properties. The devices using amorphous semiconductors were commercialized by utilizing them in fabricating electronic and optical devices to store information. The conventional crystalline semiconductors were already the most popular in the fabrication of electronic devices. Amorphous semiconductors, with the help of well-established crystalline counterparts, extend the new frontiers of research and show promising technological implementation. Such amorphous semiconductors are prepared by melt quenching and condensation from the gas phase. In the melt quenching from liquid, the melt of a liquid is supercooled and the material undergoes a transition to the glassy phase at a particular temperature called glass transition temperature (T_g). Condensation from the gas phase is technique in which the vapor phase of the materials are deposited on a substrate. There are many different techniques for deposition of amorphous materials such as physical vapor deposition (PVD), chemical vapor deposition (CVD), sputtering and etc.

Bombardment of ionizing particles on to the crystalline semiconductors can also amorphize the materials [2].

The physics of a-Semiconductors is understood in terms of their basic nature in crystalline state. In the crystalline state of Si, it is four fold coordinated, i.e. each Si is surrounded by other Si atoms by the covalent bonds. In the same away, in amorphous state silicon is surrounded by four other Si atoms, with no long range ordering. Few atomic sites possess its regular four-fold coordination as in crystalline Si and few other sites are under or over coordinated. Amorphous semiconductors are characterized by different bond lengths, bond angles and different coordination in various atomic sites. The introduction of three-fold coordination creates uncompensated bonds, called dangling bonds. Because of the disorder in a-semiconductors, there are weak, strained and uncoordinated dangling bonds formed. The electrons associated with these strained bonds and uncoordinated dangling bonds form the tail states, which lie in the forbidden region of the band diagram, mostly above and below the extended states. The electrons that occupy these states are localized. In a c-semiconductor, there is well-defined energy gap between valence and conduction bands. Because of the presence of tail states in a-semiconductors, energy gap in a-semiconductors is not well-defined. Below figure gives the schematic illustration of energy bands in both crystalline and amorphous semiconductors.

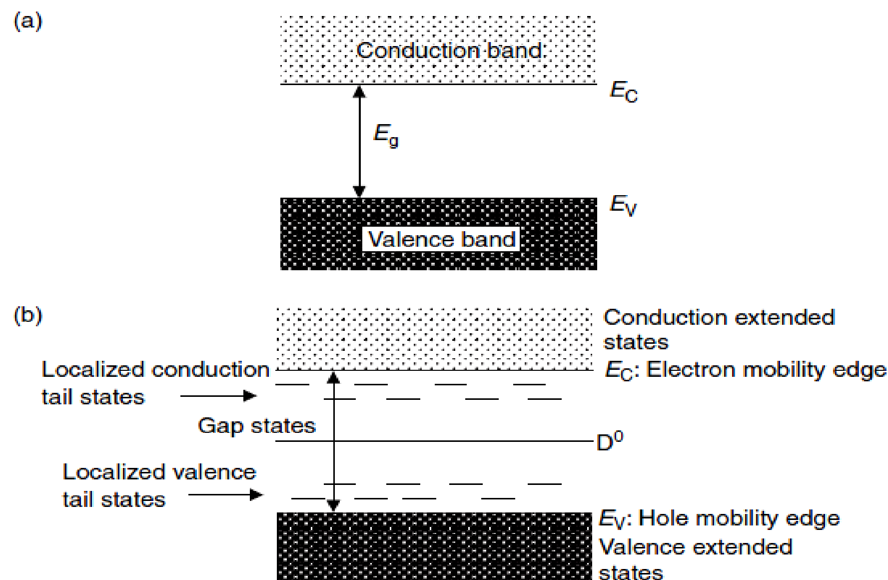

Fig 2.1.1.1: (a) Schematic illustration of energy bands in c-semiconductors. (b) Energy states in amorphous semiconductor. Image is reproduced from reference [2].

The tail states close to the valence band edge and conduction band edge give rise to the formation of acceptor and donor levels respectively. The edges separating the extended and localized states are called mobility edges. So, there are two mobility edges: upper

mobility edge or the electron mobility edge, which separates the conduction extended states and tail states below the conduction band and the lower mobility edge or the hole mobility edge, which separates the valence extended states and the tail states above the valence band. The typical density of states for an a-semiconductor is illustrated in the below figure.

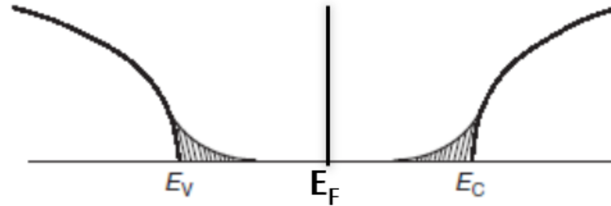

Fig 2.1.1.2: The schematic illustration of density of states in a-semiconductors. The image is reproduced from reference [2].

The energy gap for a-semiconductors is not well defined because of the presence of tail states which are present in the forbidden region. Because of the presence of high density of tail states, a-semiconductors are insensitive to doping and they don't exhibit photoconductivity. The tail states in the mid gap position act as trapping and recombination centers for the electrons which are made free from the extended states. Thus, amorphous semiconductors act as intrinsic semiconductors with poor conducting properties.

2.1.2 Electrical conduction in amorphous semiconductors

It is well known that the disorder in amorphous structure causes the tail states which lie in between the energy gap E_c - E_v. These tail states exponentially decrease from their mobility edges. Because of the presence of high density of tail states, a-semiconductors do not show any effect on doping and since these localized states act as traps and recombination centers and don't exhibit photoconductivity [2].

To make a-semiconductors conducting, we should think of the mobility of the charge carries which occupied the tail states. As explained by Mott and Davis [3], there is a mechanism called "Variable range hopping" responsible for the conduction between the tail states. Since the atoms associated with dangling bonds are distributed randomly in a disordered structure and there are plenty of such states, there is a continuous hopping path between the states which differ in their energy levels. Hence, the hopping is a thermally activated phenomenon. As explained by Mott, the relationship between conductivity σ and temperature T, A-exponential constant, is given by the following expression [3, 4].

$$\sigma \; \alpha \; \exp(-A/T^{1/4}) \quad \ldots\ldots.\;\ldots\ldots\ldots\ldots\ldots \; 2.1$$

It is also pointed out that there is a plausible tunneling mechanism involved in the conduction of electrons between the traps present, when they are sufficient in number [4]. In a-semiconductors, with the application of voltage before switching there is a linear increase in current due to space charge region formed between the electrode and the material [5]. At the switching voltage, there is an exponential increase in current because of the delocalization of tail states by reducing the mobility gap [5, 6]. The electrical break down occurs at this switching voltage causing a rapid increase in carriers emitted from the valence band and localized tail states to conduction band which leads to an exponential increase in current [5].

2.2 Chalcogenide semiconductors for phase change memory

The crystalline Si or Ge semiconductors have covalent networks of rigid diamond cubic structure. Due to these strong covalent networks, they have high melting temperatures: Tm of 952 ˚C for Ge and 1414 ˚C for Si. Because of the high melting temperatures, it is difficult amorphize c-semiconductors and on the other hand it is difficult to crystallize the a-semiconductors due to their high viscosity [7].

In case of chalcogenides such as Te and Se, they are two-fold coordinated and exhibit coil like structures. Each two-fold coordinated Te coil like structures are bound by other coil like structures by the weak vanderwall forces and forms a hexagonal crystal structure. Because of the presence of weak vanderwall forces that connect the Te-coils, Te has a low melting temperature (T_m = 450 ˚C). Therefore, Te in its melt state possess two-fold coordinated structure. The rapid quenching of this melt can lead Te to have few three fold coordinated sites with Te coil structures. The amorphous Te is not stable even at room temperature, because of the existing 3-fold coordinated atomic sites and they tend to lose their bond with one of the Te's and form a crystalline Te. Below is the figure shows the amorphous and crystalline Te networks. To get a stable amorphous Te, we need to add elements which can cross-link with Te coils strongly. Three fold and four fold coordinated elements such as As, Sb, Ge and Si etc. The four fold coordinated elements like Si and Ge will form cross-linking bonds with Te coil like structures and make low melting point compounds and easily become crystalline from their melt and there amorphous phase is stable [7].

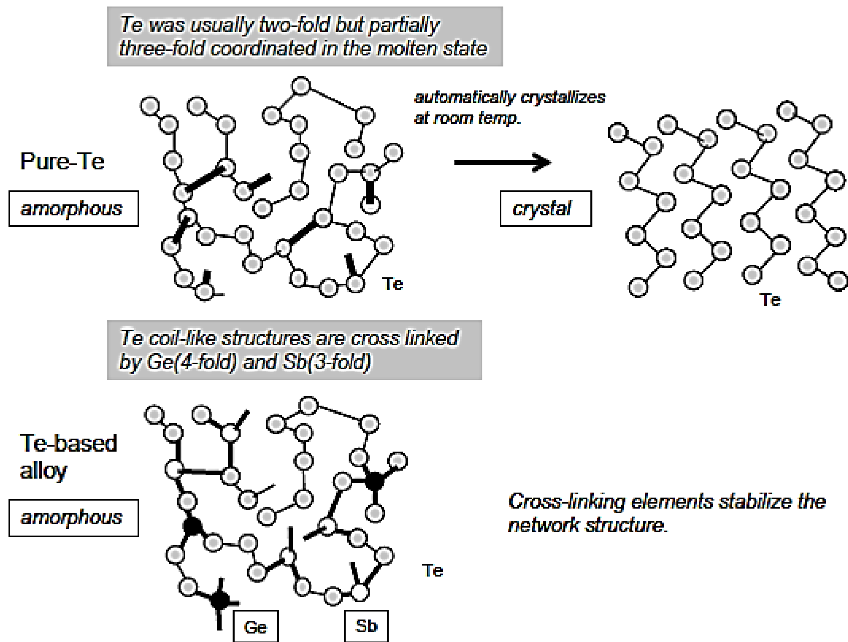

Fig 2.2.1: Schematic of atomic configuration of Te in amorphous and crystalline state (top). Amorphous Te with the addition of cross-linking elements (bottom). Image is reproduced from ref [7].

2.3 Ge-Te system

Stoichiometric GeTe is a member of Ge-Te system, which exhibits a melting temperature of 998 ± 3 K [8]. Fig 2.3.1 shows the phase diagram of Ge-Te system with respect to the variation of at. % of Te.

There are three polymorphous structures of GeTe: high temperature cubic NaCl phase (β) (space group F3m) stable at temperatures above 640 – 700 K. and two low temperature phases: rhombohedral (α) (space group R3m) and rhombic phase (γ) (structure type: SnS). Two eutectic compositions exists in binary Ge-Te system: one is at 49.85 at. % of Te and the other is at 85 at. % of Te.

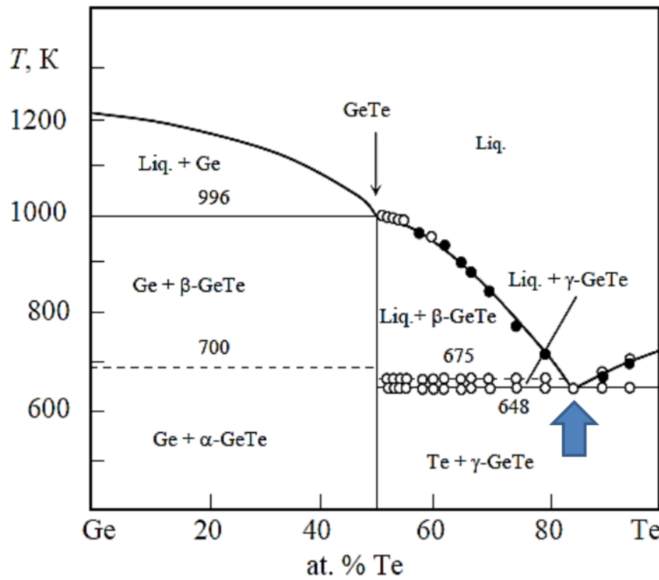

Fig 2.3.1: Phase diagram of binary Ge-Te system. Image is reproduced from reference [8].

At 49.85 at. % Te, M.P = 996 K. Liq. GeTe → Ge + β – GeTe

At 85 at. % Te, M.P = 648K. Liq. GeTe → Te + γ – GeTe

For the compositions below the 49.85 at. % of Te, the materials will have precipitation of Ge in their solid solution of GeTe and for the compositions above 51.5 at. % of Te, materials will have Te precipitates with the solid solution of GeTe up to a temperature of 648 K. Rhombohedral modification is stable in the composition range of 50.3 to 50.5 at. % of Te, rhombic phase is stable in the range of 50.9 to 51.2 at. % of Te and the high temperature cubic phase is stable in the range of 50.3 to 51.2 at. % of Te. Slow cooling of β-phase leads to a rhombic GeTe and the rapid cooling of cubic GeTe leads to a rhombohedral phase [9].

2.3.1 GeTe as a phase change memory material

At room temperature, the stoichiometric GeTe possess a rhombohedral structure with space group R3m and lattice constants a = 4.21 A˚ and c = 10.6 A˚ (hexagonal setting). The GeTe lattice can be seen as a distorted rocksalt structure with Ge and Te locate on the fcc sublattices. The lattice undergoes a distortion along the [111] direction with an angle of α = 88.35˚ deviating from 90˚.

In GeTe, each atom is octahedrally coordinated by forming three longer bonds (3.158 A˚) and three shorter bonds (2.843 A˚) because of the distortion of the two

sublattices. Since Ge and Te don't have enough number of electrons to form six covalent bonds, it is understood that few bonds in GeTe are resonant bonds which are weak and long.[7] From the phase diagram mentioned earlier, it is also clear that the room temperature stoichiometric rhombohedral GeTe undergoes a structural phase transition to cubic GeTe at ~ 420 ˚C.

From Extended X-ray Absorption Fine spectrum (EXAF) studies, the amorphous structure of GeTe is found to be consisting of Ge(4): Te(3) with a small contribution from Ge(3):Te(3). Most of the structural units have 4-fold coordinated Ge atoms with 3-fold coordinated Te atoms. Upon the transformation from crystalline to amorphous GeTe, the Ge changes from an octahedral atomic site to a tetrahedral atomic site by breaking its weak resonant bonds. The covalent bonds become stronger in amorphous GeTe by reducing their bond length to 2.6 A˚. These substantial changes in the bond length and the type of bonding in both amorphous and crystalline phases of GeTe cause a significant difference in its electrical and optical properties [7, 9].

Among all the possible materials in Ge-Te system, the stoichiometric GeTe (50 at.% of Ge and 50 at.% of Te) is an active material employed in phase change memory devices which is proven to be better compared with other successful materials such as $Ge_2Sb_2Te_5$. GeTe exhibits a better resistance contrast of more than three orders of magnitude and this contrast is stable up to 1×10^5 cycles. It has shown a laser induced crystallization time of 30 ns. Data retention characteristics are found to be stable up to a temperature of 165 ˚C without altering any data [10].

Moreover, the phase diagram illustrates that the eutectic composition of GeTe system, i.e. $Ge_{15}Te_{85}$, often reported as $GeTe_6$, shows the lowest melting point which provides low operating requirements to be utilized in phase change memory. Deviation of composition from the stoichiometric GeTe makes significant changes to its electrical properties.

2.3.2 $Ge_{15}Te_{85}$

$Ge_{15}Te_{85}$, also called as $GeTe_6$ is a eutectic composition of GeTe binary system which has a lowest melting point (~648K) than all other compositions existing in GeTe system. The two phases existing in this composition are: Hexagonal Te and rhombic GeTe phases [8].

Differential scanning caloriemetry (DSC) results proved that $GeTe_6$ powders exhibit a two-stage crystallization due to the phase segregation of Te and subsequent formation of GeTe crystallites at 210°C and 230°C respectively [11]. The dual stage crystallization in amorphous $GeTe_6$ is expected to arise, due to the presence of excess of Te, which are not bound to Ge [12]. In the amorphous structure of $GeTe_6$, each Ge is coordinated by four Te atoms and each Te has no Ge neighbor in their first coordination sphere and it is described by $GeTe_4$ tetrahedra as structural units which are interconnected by Te-Te bonds [12]. Due to the dual stage crystallization, the crystallization time are relatively higher in $GeTe_6$ and was found to be ~100μs [7, 13]. Because of the high crystallization time, it was never used as a phase change memory element. But, the recent investigations on $GeTe_6$ explained that it can be used as an ovonic threshold switch (OTS) selector device which can be integrated with a phase change memory cell [14].

OTS selector device:

OTS device is an electronic switch, used to access a memory bit in a memory array by the application of a sufficient voltage. Since it is used as a switch for a memory cell, it can be used to write, erase and read the information of a memory cell without losing its characteristics during the operation.

The studies of characterizing an OTS device were carried out by subjecting to different voltage pulses and the device under test (DUT) was fabricated in the conventional bottom heater geometry as shown in the below figure.

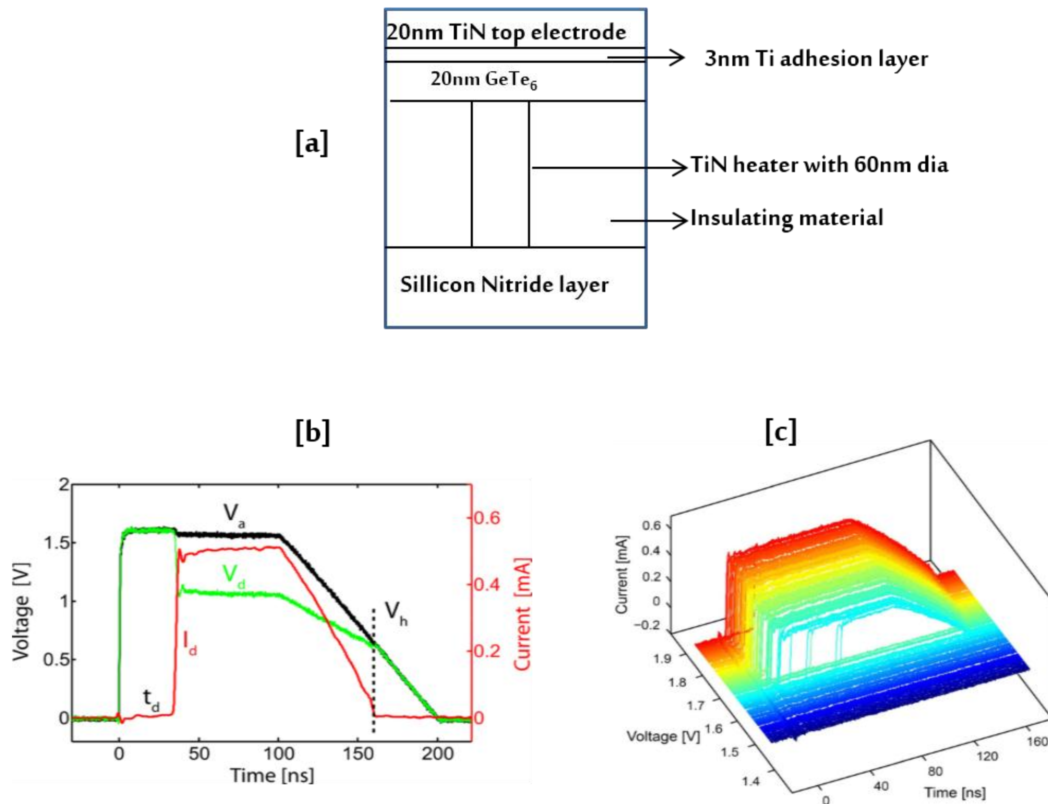

Fig 2.3.2.1: [a]. Schematic of the device under test (DUT). [b]. Time resolved measurements of threshold switching characteristics for an OTS device measured with an applied voltage of 1.4 V. [c]. Time resolved measurements for voltage pulses ranging from 1.4 V to 1.85 V. Image is reproduced from reference [10].

The electrical characterization performed on $GeTe_6$ OTS selector device exhibited a threshold switching with applied voltages in a range between 1.40 V and 1.85 V with no appreciable change in the holding voltage, but with a strong dependence of delay time. It is also found that the conducting 'ON' state current of 650µA serve as the sufficient reset current for different PCM cell structures without modifying its switching characteristics [14]. The holding voltage of the OTS device is found to be stable over a range of applied pulses showing the stability of the device. The least possible switching delay for the device is found to be ~5 ns, suggesting faster switching. The reproducibility of the switching states with constant holding voltage was seen for 600 pulses. Slight increase in the threshold switching was observed after 600 pulses and is thought to be the result of the modifications in the local structure which results from the thermal annealing of the material resulted either from the conductive 'ON' state current or the additional heat produced by the TiN heater embedded in the memory cell [14]. Since, the problem of phase segregation of Te affects the

switching characteristics and their associated crystallization behavior; the measurements at nanoscale widen the plausible integration of $GeTe_6$ switch along with a GeTe memory cell.

2.4 Motivation to the present work

Since it is understood that $GeTe_6$ phase change material possesses high crystallization time because of the phase separation of Te. But from the recent investigations reported in [10], it is evident that $GeTe_6$ PC material can be used as an OTS selector device. But the property enhancement of numerous switching times is not achieved, which is assumed to be an effect of phase separation. Such nanoscale structural modifications are though difficult to study practically, C-AFM studies on this material can make out the real problem of phase separation which associated with the indifferent electrical contrast. The dual phases present in the $GeTe_6$ can also strongly influence the programming characteristics, since they exhibit two different electrical properties. The motivation of the present work is to study the nanoscale local electrical properties of $GeTe_6$, which is being in amorphous and crystalline phases to detail the influence of phase separation on device characteristics.

2.5 Objectives of the work

The objectives of the work are:

1. To apply different biasing voltages to find out the threshold switching and memory switching behavior of GeTe6.
2. To probe a phase change region or memory switched region with low biasing voltages and to confirm the memory switching
3. To check the stability of memory switching events with multiple number of I-V ramps and studying their dependence on delay time.
4. To make large area scans so that the variation in electrical contrast can be visualized as the existence of different phases.
5. To apply small biasing voltages to check whether there is any remarkable difference in the current in current mapping image to find out the phase separated region.
6. The phase separation stimulated by thermal annealing at a particular favorable temperature is benefitted to understand the lone phase of phase separated Te embedded in amorphous material.

References

1. Ovshinsky, Stanford R. "Reversible electrical switching phenomena in disordered structures." Physical Review Letters 21, no. 20 (1968): 1450-1453).
2. Advances in condensed matter science: Edited by D.D. Sarma, G. Kotliar and Y. Tokura, Taylor & Francis, 2003.
3. Myers, H. Peter. Introductory solid state physics. CRC Press, 1997.
4. Nevill, Mott. "Conduction in amorphous materials." Electronics & Power 19, no. 14 (1973): 321-324.
5. Fritzsche, Hellmut. "Why are chalcogenide glasses the materials of choice for Ovonic switching devices?." Journal of Physics and chemistry of Solids 68, no. 5 (2007): 878-882.
6. J. Frenkel, The Journal of Experimental and Theoretical Physics USSR 8 (1938) 1242.
7. Raoux, Simone. Phase change materials. Springer, 2009.
8. Bletskan, D. I. "Phase Equilibrium in binary systems AIVBVI." Journal of Ovonic Research Vol 1, no. 5 (2005): 47-52.
9. Bogoslovskiy, N. A., and K. D. Tsendin. "Physics of switching and memory effects in chalcogenide glassy semiconductors." Semiconductors 46, no. 5 (2012): 559-590.
10. Perniola, Luca, Veronique Sousa, Andrea Fantini, Edrisse Arbaoui, Audrey Bastard, Marilyn Armand, Alain Fargeix et al. "Electrical behavior of phase-change memory cells based on GeTe." Electron Device Letters, IEEE 31, no. 5 (2010): 488-490.
11. Hoyer, W., I. Kaban, P. Jóvári, and E. Dost. "Crystallization behavior and structure of amorphous $Ge_{15}Te_{85}$ and $Ge_{20}Te_{80}$ alloys." Journal of non-crystalline solids 338 (2004): 565-568.
12. Kaban, I., Th Halm, W. Hoyer, P. Jóvári, and J. Neuefeind. "Short-range order in amorphous germanium–tellurium alloys." Journal of non-crystalline solids 326 (2003): 120-124.
13. Chen, M., K. A. Rubin, and R. W. Barton. "Compound materials for reversible, phase-change optical data storage." Applied physics letters 49, no. 9 (1986): 502-504.
14. Anbarasu, M., Martin Wimmer, Gunnar Bruns, Martin Salinga, and Matthias Wuttig. "Nanosecond threshold switching of GeT_e6 cells and their potential as selector devices." Applied Physics Letters 100, no. 14 (2012): 143505-143505.

Chapter – 3

Experimental Details

This chapter details the preparation of thin films and the characterization of as-deposited thin films. The preparation of thin films plays an important role, which determines the microstructural and other physical properties to be analyzed. In the present work, the thin films were prepared by dc magnetron sputtering method [1, 2] and several characterization techniques are employed to investigate the electrical properties.

The sputtered $GeTe_6$ thin films were received from Dr. Anbarasu M, currently a faculty in the department of electrical engineering, IIT Indore. These films were processed under Argon atmosphere with a pressure of 5x10-6 mbar and a flow rate of 20 s.c.c.m, operated in constant power mode of 20 W. The films were deposited on SiO_2 (20 x 20 mm) substrates from a single $Ge_{15}Te_{85}$ target of 99.99% purity (Target supplied by Umicore, Germany) with a deposition rate of 0.098 $nm.s^{-1}$. The thickness of the films is 200 nm.

3.1 Scanning electron microscopy (SEM)

Scanning electron microscope (SEM) is one of the most potential instrument to study and analyze the microstructure, morphology and chemical compistion of materials. SEM makes use of highly focussed and energetic electrons that scans across the material. The electron beam interacts with the sample and gets the signal from the surface and the interior of the material which gives the information about morphological, chemical composition and other properties.

The major components of the SEM are: Vaccum system, Beam generation system, Beam manipulation system, Beam-specimen interaction system, Detection system, signal processing and display and recording system [3]. The schematic diagram of a typical SEM setup is given in the below figure.

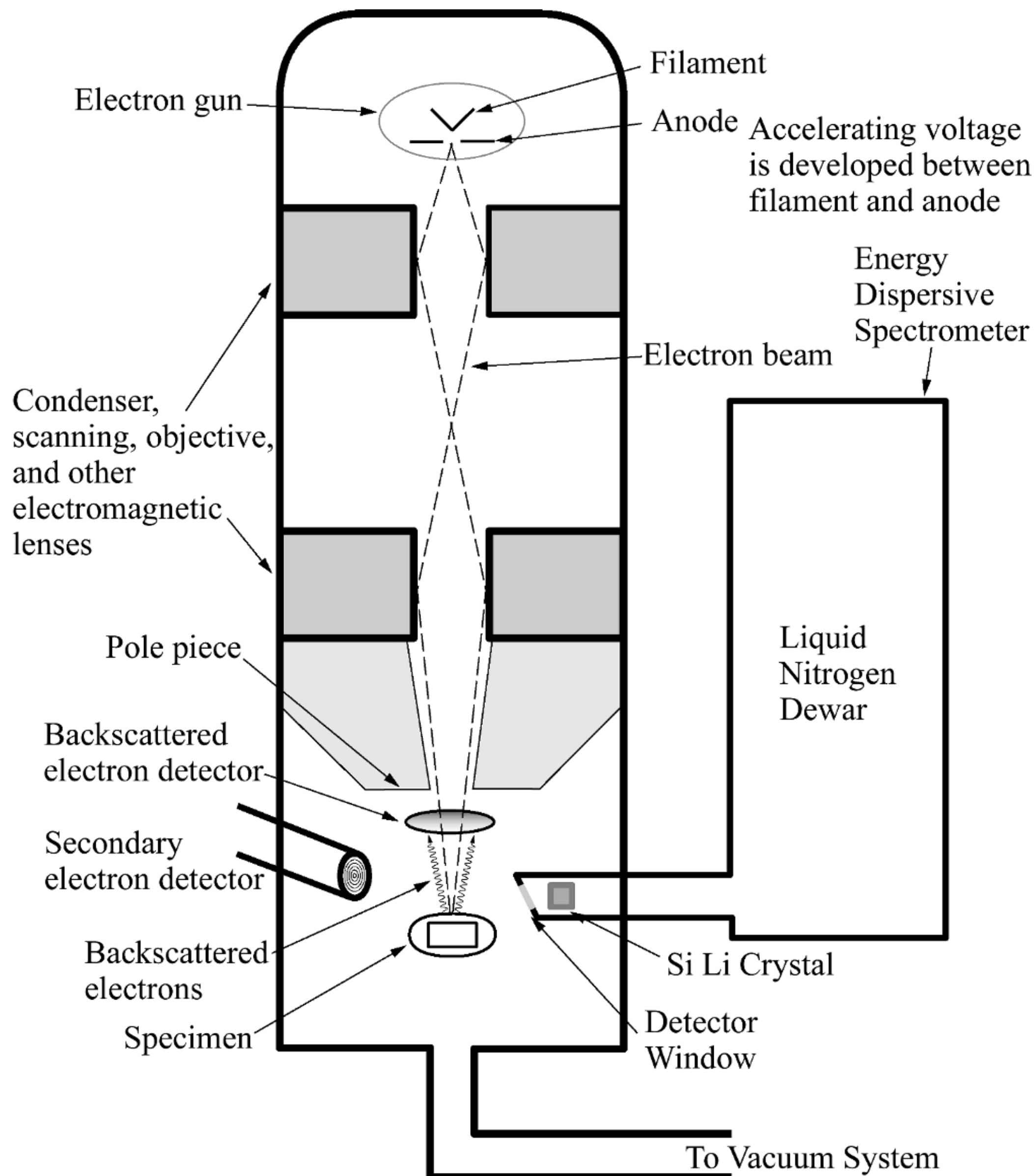

Fig 3.1.1: Schematic of typical SEM setup equipped with EDS. Image is reproduced from reference [3]

The image formation in SEM depends on the acquisition of the signals, acquired from the interaction of the specimen and the sample. Based on the energy loss of the incident electron beam, the interactions are classified into two categories: Elastic and Inelastic scattering [3]. In the Elastic scattering, the electron beam which incidents on the specimen, bounces back off the sample with an angle more than 90˚ with a negligible energy loss to the specimen. This electrons of wide angle scattering are called as back scattering electrons (BSE) and they possess the energy of about 50 eV. Generally, 10-50% of incident

electrons are BSEs and they possess 60-80% of their initial energy. The image formed utilizing the BSEs contains the information about the composition and topography [4]. The schematic of electron beam and specimen interaction is given below.

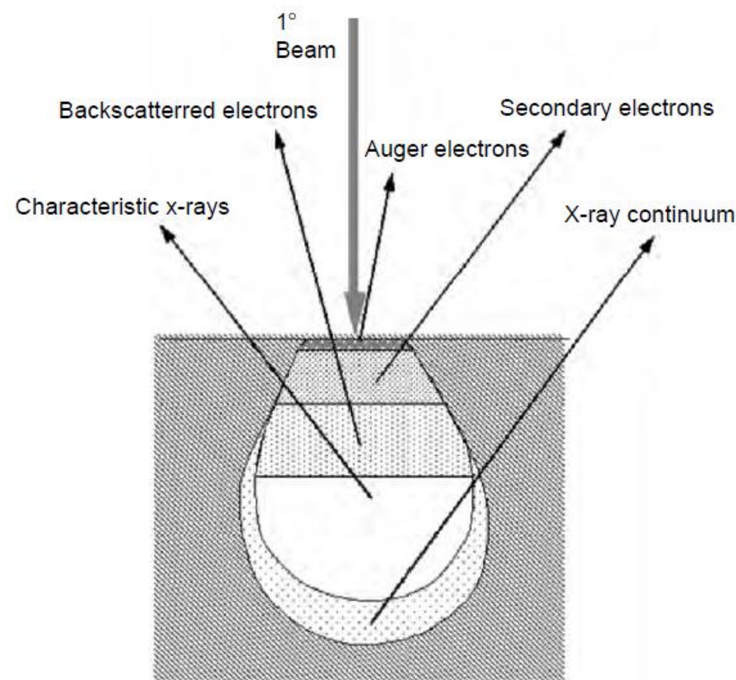

Fig 3.1.2: The illustration of different signals produced by the electron beam and the specimen interaction in SEM. The image is reproduced from reference [4].

In inelastic scattering, there are a variety of signals produced. They are: Secondary electrons, characteristic X-rays, Cathodoluminescence and Auger electrons.

Secondary electrons:

Secondary electrons (SE) are generated when the incident or primary electron beam strikes the surface and causes the ionization of specimen atoms. Since, the SEs possess lower energy ranges from 3-5 eV, it is easily grabbed by the detector. SE signal is acquired from a region within a few nanometers of the surface. SE signal is the most useful signal for studying the topography of surface [4].

Characteristic x-rays:

When the primary electron beam interacts with specimen atom by displacing its inner shell electron with the outer shell electron, X-ray photon is emitted. This is called as Characteristic X-ray signal. In addition to the characteristic X-ray, there would be a background noise generated, when the primary electron beam makes a series of interaction

with different atoms by losing its energy, it will form a signal called Bremsstrahlung or continuum X-rays. This is a noise signal, which is usually stripped from the data before analysis. Characteristic X-rays possess a particular energy depending on the transition between the orbitals and the atomic number, it gives the information about chemical composition [4].

Auger electrons:

When the primary electron beam strikes the specimen atom and dislodges a electron from a core shell, the vacancy is filled by another electron from a high energy orbital releasing an energy equals to the energy difference of both of the orbitals. If an electron from a high energy orbital captures this energy and is removed off the atom, the electron is called auger electron. Since this electron has a characteristic energy depending on the transition between orbitals, chemical composition of the specimen can be determined using auger electron signals. Auger electron signals are captured within few nanometers below the surface since they possess low energies [4].

Cathodoluminescence:

When the primary electron strikes the specimen, electrons in the atom gains energy and transit to conduction band leaving a hole behind. These electrons will recombine with the hole to emit photons. This is called luminescence. Different specimens release photons of different wavelengths [4].

3.1.1 Energy dispersive X-ray spectroscopy (EDS)

Energy dispersive X-ray spectroscopy is the powerful technique to study the chemical composition of materials, which is attached to SEM. In EDS, characteristic x-rays emitted from the material are analyzed to determine the chemical composition.
The most commonly used EDS detector is Lithium drifted Sillicon detectror (Si(Li)) [5]. For a detector material we need to have pure intrinsic semiconductor which doesn't have any charge carriers. But, in practice it is difficult to obtain pure semiconductor. So, Lithium (a n-type dopant) is joined to a p-type sillicon to compensate the charge carriers in sillicon. By joining the two, the p-n junction becomes intrinsic, which is a few microns thick. By applying a reverse bias to the p-n junction, the thickness of intrinsic region will be increased. This is called as lithium drifted sillicon. Since, Lithium is mobile at room temperature, it is important to operate the detector in liquid nitrogen temperatures. In a Si(Li) detector, the lithium drifted sillicon crystal is placed between two electrodes [5].

When a X-ray photon is emitted from the specimen and falls on the detector, x-ray photon energy is absorbed by the crystal. Photoelectrons are ejected from the crystal and lot of electron-hole pairs are formed by utilizing the x-ray energy until the x-ray photon energy is dissipated in the crystal. This electrons and holes are attracted towards the electrode and this charge is converted to voltage by a charge to voltage converter. By multiplying the values of the number of charge generated and the average energy for a single electron-hole formation will give the energy of x-ray (in eV) phonton incident on the detector. The voltage output from a charge to voltage converter is further amplified and given to a computer x-ray analyzer, which displays the information of energies (in keV) in a histogram pattern [5].

.

LaboratoryInstrument:

The laboratory instrument we have utilized for the present investigation is given in the below figure.

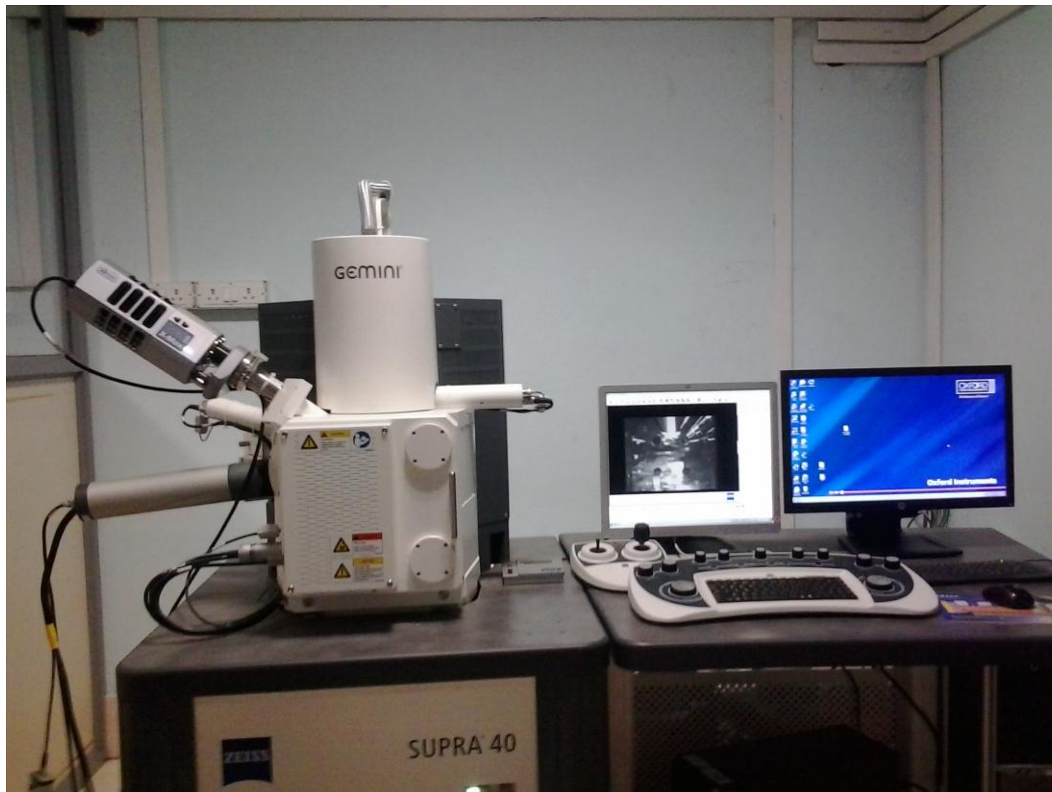

Fig 3.2.1.1: The laboratory instrument used for SEM-EDS measurements for compositional analysis.

In the present study, the compositional analysis of $GeTe_6$ phase change thin films was performed by using SEM-EDS (make: CARL-ZEISS). The $GeTe_6$ thin film was mounted on the sample holder using carbon tape and inserted in to SEM chamber to proceed

for EDS analysis. High vaccum of 5 $\times$ 10^{-5} mbar is maintained inside the chamber. To carry out EDS maeasurements, the scan parameters maintained are: a) Magnification - 5000 b) Accelerating voltage – 20 kV c) Working distance – 10 mm

3.2 X-ray powder diffraction

X-rays are electromagnetic waves, possess the energy ranging from about 100 eV to 10 MeV. The wave length of x-rays ranges from 10^{-3} nm to 10 nm. Since, it is an electomagnetic wave, it is characterized by an electric field vibrating perpedularly to its direction of movement. When an X-ray beam of wavelength equals to the interatomic spacing moves through a material (collection of atoms seperated by a specific distance), it can get scattered by electron cloud of atoms. This scattering of X-rays or X-ray diffracton was first discovered in copper sulphate crystal and the diffraction pattern was recorded on a photographic plate by Laue, Friedrich and Knipping in Munich in 1912 [6]. Further, X-ray diffraction technique was developed by W. H. Bragg and W. L. Bragg. Nowadays, X-ray diffraction technique became the most widely used analytical technique to characterize the structure of the materials .

X-ray diffraction is a scattering phenomenon from a periodic arrangement of atoms in a lattice. All the scattered rays from atoms can't contribute to a diffraction pattern. There is a definite phase relation between the scattered rays to be constructively interfered to form a diffraction pattern, which is explained by Bragg's law of diffraction [6].

3.2.1 Bragg's Law

In 1913, W L. Bragg first gave the mathematical explanation for X-ray diffraction. To understand the Bragg's law, consider a wavefront of x-rays incidenting on a series of crystallographic planes as shown in the below figure 3.3.1.1.

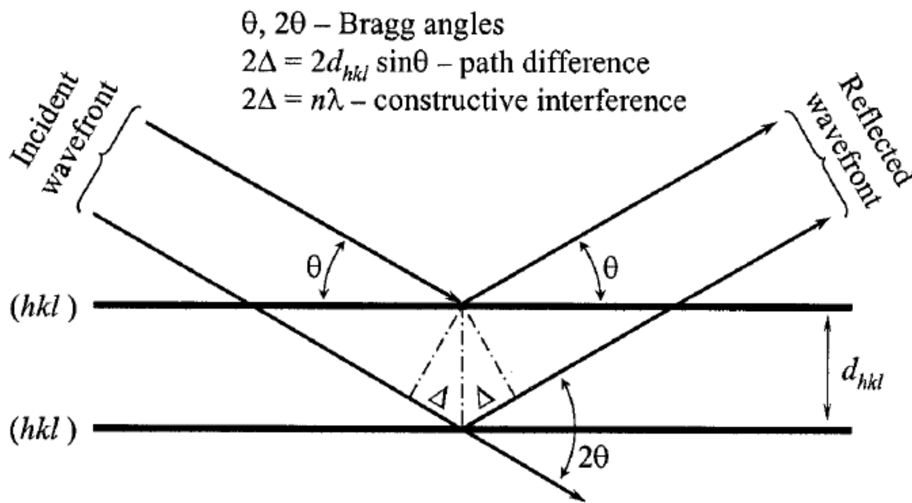

Fig 3.2.1.1: Schematic diagram of X-ray diffraction by a crystal. Image is reproduced from reference [7].

Two parallel x-rays are incidenting on the parallel planes seperated by a distance "d". These parallel planes act as X-ray reflectors. The reflected X-rays can be coherent or incoherent, which depends on the phase of the x-ray, which indirectly depends on the path difference between the two rays. If the x-rays are coherent, there is a constructive interference which can form a diffraction spot and if the reflected x-rays are not coherent, they destructively interfer which does not give any diffraction spot. So, for a diffraction pattern to occur, the path difference between the reflected rays should be integral times of λ [7]. From the above illustration, the path difference is 2Δ.

$$2d_{hkl}\sin\theta = n\lambda \qquad \text{...... ..3.2.1}$$

The above eqn is called Bragg's law of diffraction. In the above eqn, d_{hkl} is the interplanar spacing, λ is the wave length of x-ray and n is the order of reflection. Since, the value of sinθ doesn't exceed unity, the above eqn can also be written as

$$\frac{n\lambda}{2d} = sin\theta < 1 \qquad \text{....... ......3.2.2}$$

From the above eqn, nλ should be less than 2d. For a small value of n (i.e., n = 1), λ must be less than 2d. So, for a diffraction pattern to occur, the wavelength of x-rays (typically less than 6 A°) used must be less than twice of the interplanar spacing (d) [6].

$$\text{i.e., } \lambda < 2d \qquad \text{............ 3.2.3}$$

From the above pictorial explanation, The angle between the transmitted beam and the diffracted beam is always 2θ. This is known as diffraction angle which is measured during the experiment.

With the known values of wave length (λ) and the diffraction angle (2θ), one can find out the d-spacing between a particular set of planes of a crystal from which the diffraction pattern is obtained [6].

For a cubic structure, if the lattice parameter is 'a' with interplanar spacing 'd' of a set of planes indicated by (hkl) then the relationship between interplanar spacing and the lattice parameter is given by,

$$\frac{1}{d^2} = \frac{h^2+k^2+l^2}{a^2} \qquad \text{……… 3.2.4}$$

By combining equations 3.3.2 and 3.3.4, then

$$\sin^2\theta = \frac{\lambda^2}{4a^2}(h^2+k^2+l^2). \quad \text{……...3.2.5}$$

Each crystalline material has a unique diffraction pattern. The set of planes of a particular crystal structure that could contribute to diffraction pattern is mathematically derived from the structure factor calculations [8]. Mathematically, structure factor is expressed by F_{hkl} and is given by the folllowing expression.

$$F_{hkl} = \sum_{j=1}^{n}\left(f_j e^{2\pi i(hu_j+kv_j+lw_j)}\right) \quad \text{…… 3.2.6}$$

It gives the sum of the of the scattered waves from the atoms of a unit cell of a particular crystal structure. If $F_{hkl}= 0$, then it means that the scattered waves are contributing to a destructive interference and if $F_{hkl}\neq 0$, then it means that the scatted waves from the atoms are contributing to a constructive interference which satisfy the bragg's condition. From the structure factor calculations of different crystal structures, we can find the possible allowed reflections from the planes which give a diffraction pattern. Below is the table gives the possible allowed reflections from the planes of a particular crystal structure.

Table 3.2.1: Relationship between the bravais lattice and reflections from their planes [8].

Crystal type	Bravais Lattice type	Reflections possible present	Reflections necessarily absent
Simple	Primitive	Any h, k, l	None
Body-centered	Body-centered	$h + k + l$ even	$h + k + l$ odd
Face-centered	Face-centered	h, k and l unmixed	h, k and l unmixed
Diamond cubic	Face-centered cubic	As fcc, but if all even and $h + k + l \neq 4N$; then absent	h, k and l mixed and if all even and $h + k + l \neq 4N$
Base-centered	Base-centered	h and k both even or both odd* $h + 2k = 3N$ with l even	h and k mixed*
Hexagonal close-packed	Hexagonal	$h + 2k = 3N \pm 1$ with l odd $h + 2k = 3N \pm 1$ with l even	$h + 2k = 3N$ with l odd

Apart from the crystal structure detemination, x-ray diffraction is also used for calculating the crystallite size and lattice strain.

3.2.2 X-ray Diffractometer

In the X-ray diffractometer, there are five essential parts: X-ray tube, incident beam optics, goniometer, receiving side optics and detector. The schematic of the laboratory instrument used is given in the figure 3.2.2.1. X-rays produced in x-ray tube pass through the optics and focussed on to the sample. X-rays hit the sample surface and get scattered from the surface and the diverged x-ray beam from the surface is detected by the detector. Goniometer is the combined set up that include the x-ray tube, sample holder and the detector. The movement of all these components are mechanically coupled. In a theta-2theta goniometer configuration, x-ray tube is kept stationery, while the sample holder moves by an angle of theta where the detector arm simultaneously moves by an angle of 2theta.

In a theta-theta goniometer configuration, the sample holder is kept stationery and horizontal to the surface and the x-ray tube and the detector arm move contemporarily with the same angles.

Fig 3.2.2.1: The laboratory instrument used X-ray diffraction studies for structural analysis.

In the present investigation of $GeTe_6$, Panalytical X'pert pro diffractometer was utilized for structural analysis. The instrument parameters are: a) Goniometer configuration – theta/theta b) X-ray radiation – Cu-K_α – 1.54 A° c) Power supply – 230 V, 50 Hz d) Sample holder – Glass slide. Scanning parameters are: a) Scan speed - b) Step size - c) Increment

3.3 RAMAN SPECTROSCOPY

Raman spectroscopy is based on the inelastic scattering of light through the matter which was first explained by Smekal in 1923 and experimentally it was first observed by Raman and Krishnan in 1928. Raman spectroscopy is widely used technique to investigate the chemical structure of the materials and the amount of a substance present in the material.

When a light of photons interacts with a material, the incident photons can distort the electron cloud or it induces a dipolemoment in the molecule with the nuclear motion, which is a virtual state. If the molecule relaxes to its ground state with in no time without influencing energy of the incident photon. It is called as Rayleigh scattering. If the molecule either absorbs the energy or gives the energy to the incident photon, then it is called as

Raman scattering. That means, there would be a change in the energy of the incident photon after scattering. Typically, the atoms in a molecule are bonded with each other which are set to vibrate at a particular frequency, called vibrational frequency. Upon the irradiation of photons on a molecule, the vibrational state of a molecule can get changed to a high energy state (excited state) [9]. The below figure illustrates the Rayleigh and Raman scattering processes in a molecule.

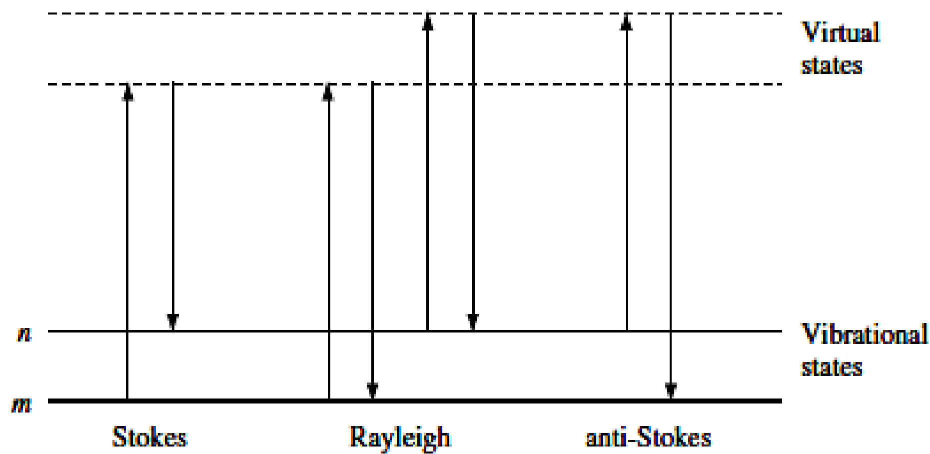

Fig 3.3.1: Schematic illustration of Rayleigh and Raman scattering processes. Image is reproduced from reference [10].

After the irradiation of the photon, vibrational state of the molecule is changed. But if the molecule gets back to its ground state or initial vibrational state within no time, there will be no change in the energy of the scattered photon. This is called as Reigh scattering. In the Raman scattering, if the molecule in the excited state gets back to a low energy state which is little higher than its ground state, then the scattered photon loses the energy. This is called as stokes scattering. But if the scattered photon gains the energy from the molecule, then it is called as anti-stokes scattering. Anti-stokes scattering is clearly explained by the figure. As depicted in figure, consider a molecule possess a vibrational state higher than its ground state because of thermal energy. Upon the irradiation by the photons, the molecule gets excited to higher vibrational energy state and after a point of time, the molecule gets relaxed to the ground state by giving energy to the scattered photon. Thus, In anti-stokes scattering, the scattered photon possess higher energy than the incident photon. From the above figure, it clear that the number of molecules that lie in a vibrational energy state above the ground state (nth state lies above mth state) at room temperature is very low.

Thus, stokes scattering is most probable and anti-stokes scattering is weak at room temperature [10].

3.3.1 Raman Spectrometer

The major components that make raman spectrometer are: Excitaion source, sample illumination and collection system, wavelength selector, detection and computer control and processing system [10].

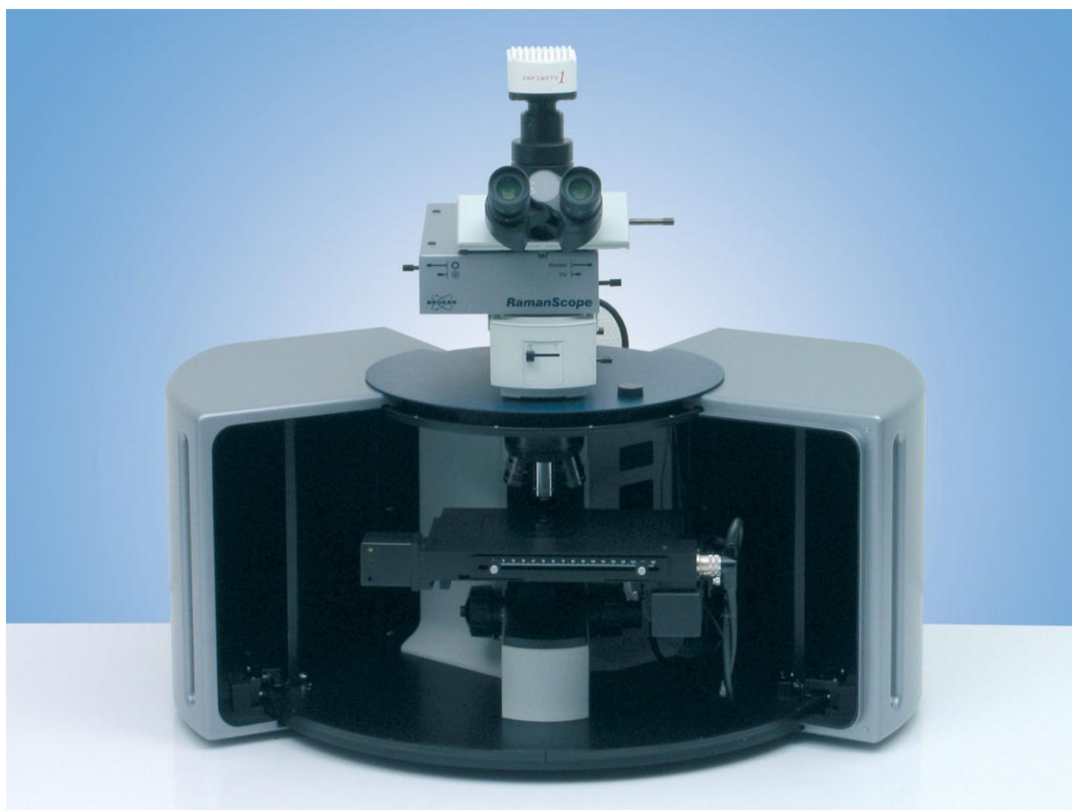

Fig 3.3.1.1: The laboratory instrument used for Raman Spectorscopy.

In the present study, Senterra, a product of Brukers is used. It is a dispersive Raman spectrometer. The multple wavelenghs available with the instrument are 532 nm and 785 nm. Instrument parameters used for current measurements are: a) Excitation source – Neon laser b) Excitation wavelength – 785 nm c) Laser power – 10 mW and 20 mW d) Time of exposure – 10 sec and 20 sec e) Spectral resolution – 3 cm^{-1}.

3.4 ATOMIC FORCE MICROSCOPY

3.4.1 History

Atomic force microscopy (AFM) is one of the family members of Scanning probe microscopy (SPM) techniques through which it was originated. Scanning probe microscope is a tool that can image nanostructures in an atomic scale. The invention of Scanning probe microscopy is considered one of the major advances in the field of material science and nanotechnology [11]. It is an instrument which studies the topography and surface properties of materials from atomic to submicron level. This invention of techniques was started with Scanning tunneling microscopy (STM) in 1981 by Gerd Binnig and Heinrich Rohrer , two physicists at IBM Research Division and their effort was awarded the Nobel prize in 1986 [11, 12]. STM probes the surface by detecting the tunneling current between metallic probe situated few angstroms above the conductive surface and the sample when an external voltage is applied. The application of STM was so particular and confined to image only conductive samples and semiconductor samples. It was overcome by the invention the atomic force microscope by Gerd Binnig, Calvin Quate and Christograph Gerber in 1986 [11, 13]. The development of AFM manifested the imaging of various surfaces in various conditions down to atomic resolution. While SPM techniques initially focused on pure imaging capabilities, the physics of probe-sample interaction and quantitative analyses of electronic, magnetic, biological and chemical surfaces have become a special interest in recent years.

The two fundamental components that make scanning probe microscopy possible are: a sharp probe and a piezoelectric scanner which is driven by a feedback control system. The sharp probe interacts with the sample surface whereas the scanner positions the probe precisely with the help of the feedback control system depending on the surface properties [11].

SPMs are a family of instruments, have been developed for various applications of scientific and industrial interest. The family of SPM techniques include Atomic force microscopy(AFM), Scanning tunneling microscopy(STM), Lateral force microscopy(LFM), Scanning electrostatic force microscopy(SEFM), Conductive atomic force microscopy(CAFM), Magnetic force microscopy(MFM), Scanning capacitance microscopy(SCM), Scanning spreading resistance microscopy(SSRM), Scanning kelvin probe microscopy(SKPM), Scanning near field optical microscopy(SNOM) and etc. Beyond imaging topography, the variety of forces between probe and sample are studied to measure

different sample properties including: surface roughness, friction, binding energies, conductivity and etc.by the use of these methods. It is clear that research and industrial applications of SPMs are expanding rapidly.

3.4.2 Introduction and Principle of Operation

The atomic force microscope was emerged as a novel technique to 3-dimensionally image the suface of the specimen by measuring extremely small forces [13]. The atomic force microscope is a technique derived from SPM methods for high resolution imaging of conducting as well as non-conducting surfaces. AFM has the advantage of imaging all kinds of surfaces including polymers, ceramics, glass, composites and biological samples whereas the STM can't image insulating materials. It merges the principles of the STM and the stylus profiler. But when compared to the stylus profiler it gives the best resolution because of its sharp probe. Like STM, the AFM scans the sample's surface and produces a high resolution 3D image by measuring the small force between the sample and the probe (rather than current in STM) predicts the precise topography of the surface [13]. The AFM techniques provide advantage over electron microscopy techniques which require sample preparation to image the specimen & also it can image the specimen in air or fluid environments rather than the utilization of high vacuum. Recently developed AFMs make the possibility of temperature control of the specimen and are equipped with a closed chamber for environment control [11].

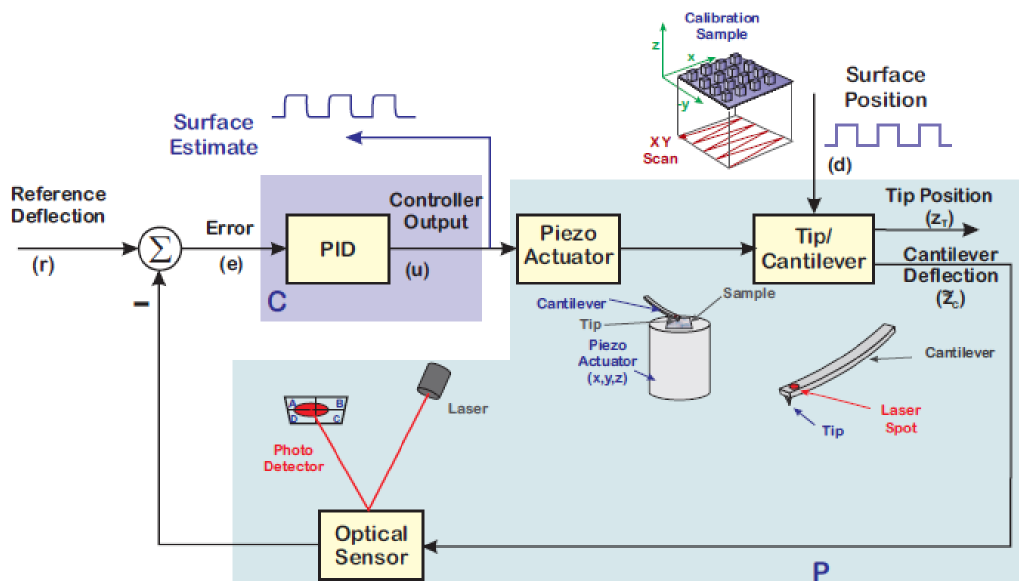

Fig 3.4.2.1: The schematic of an AFM Control Block Diagram. Image is reproduced from the ref [14]

The principle of operation of an atomic force microscopy is schematically shown in fig 3.4.2.1. A typical AFM comprises of a sharp probe which is attached to the free end of a cantilever, optical detection system consisting of a laser and a position sensitive photo detector (PSPD), a piezoelectric scanner and the feedback control system. The laser beam is made to fall on the end of the cantilever which has a reflective coating. The laser beam which falls on the cantilever bounces back off the cantilever on to the PSPD when the cantilever bends as it experiences a force from the sample. In most cases feedback mechanism is employed to adjust the probe-sample distance to maintain constant force between the probe and the sample. The piezoelectric scanner moves the sample in z-direction to maintain a constant force and in x&y-direction for scanning the sample. When the probe is brought in close proximity to the sample surface, it is affected by the forces either attractive or repulsive between the probe and sample. These forces will cause a deflection in the cantilever which can be measured with the help of optical detection system. This interaction force is always monitored as a function of the deflection or the vertical displacement traversed by the probe relative to the sample surface according to $F = k \times z$ where k is the elastic constant of the cantilever and z is the vertical displacement of the probe. . There is an optimized deflection force that feedback control electronics monitors to keep up while imaging. This is set by the instrument parameters and is called set point. The set point is characteristic for every mode [15]. Throughout the AFM operation, the interaction between probe and the sample is supervised by maintaining a constant force or constant height using the feedback control system. The deflection of the cantilever produces a continuous signal on the PSPD controls the probe-sample interaction force, subsequently manipulated by the control electronics to generate an image [14].

3.4.3 Basic Instrumentation of AFM

In general, basic instrumentation of AFM comprises of five major elements. They are cantilever-tip system, tip sample motion unit, detection unit, feedback controller and image acquisition and display system. Generally, tip sample system, tip sample motion unit and the detection unit come under a single module called microscope base [11]. The individual components that constitute the basic instrumentation is given below with the details with the of below schematic.

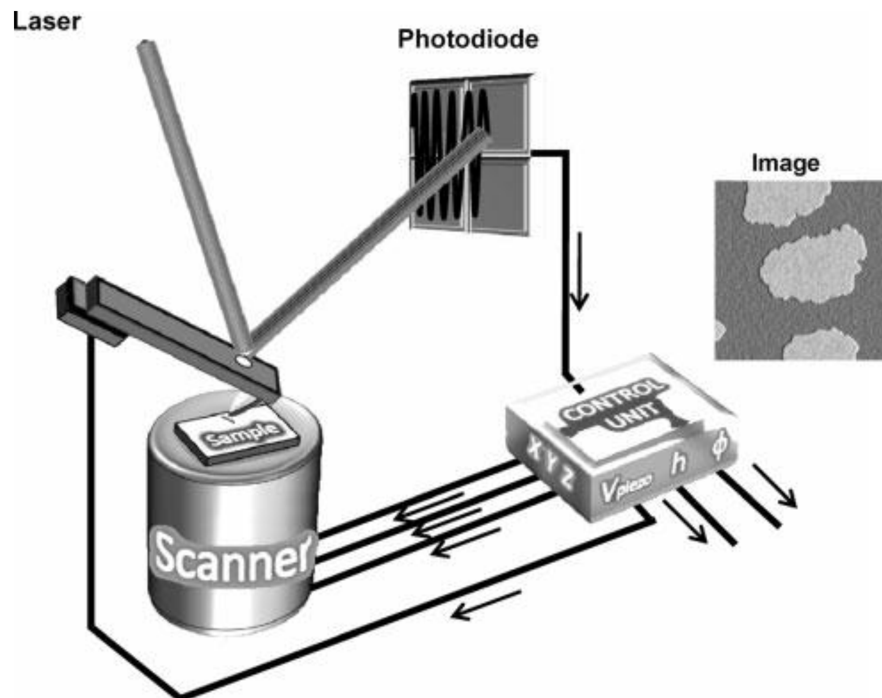

Fig 3.4.3.1: The schematic of instrumentation of atomic force microscope. Image is reproduced from ref [11].

a). Cantilever-tip system

The cantilever tip system consists of a tip and the cantilever. The tip is designed to fix at the end of the cantilever. The cantilever and the tip are integrated into a single device using the micromachining technologies such as photolithography and etching procedures. Generally, most of the cantilever are rectangular or v-shaped and they are made of either Silicon (Si) or Silicon nitride (Si_3N_4). The cantilever acts as a force transducer, since the tip attached to it experiences the force and the cantilever deflects according to that force which is recorded for the image construction [11]. Typical cantilevers have a length of 100 to 400 μm, a width of 20 μm to 40 μm and a thickness of 0.4 μm to 1 μm. The parameters that characterize the cantilever are its force constant, resonant frequency and quality factor.
The tip interacts with the sample and experience a force to cause a deflection in the cantilever. The lower the tip radius, better the resolution of the image we obtain. Standard tips have a radius down to 2 nm at the apex [11].

b). Tip-Sample motion unit

To enable the tip/sample motion during the scanning in AFM, piezoelectric actuators are used. Piezoelectric actuators position the tip/sample to a high precision of subangstrom accuracy. In AFM, piezoelectric actuators are electromechanical transducers

which convert an electric voltage into a mechanical motion. In an AFM, either the tip scans the sample by moving over the surface or the tip is stationery and the surface beneath the tip moves. Depending on the type of AFM, piezoelectric actuators position the tip or the sample along all three directions. Most commonly, tube scanners are preferred as piezoelectric electric actuators because of their compactness and high resonant frequencies. Tube scanners cover a wide range of areas from few nm2 to µm2. For better precision in the positioning, closed loop scanners are employed, which reduces the difference between the tip actual and nominal displacement during the scanning and the error signal is manipulated to a lowest possible value [11].

c). Detection Unit

The tip sample movement during the scanning has to be monitored to measure the topography. To capture the tip-sample motion, the most common method employed to measure is the optical deflection system. In optical lever detection system, a laser beam is made to incident on the backside of the cantilever which has a reflective coating. The laser beam reflects from the cantilever and incidents on a four quadrant photo diode also called position sensitive photo detector (PSPD). The PSPD captures the deflection of the cantilever when the tip scans the sample surface. Before starting the scanning, we should make sure that laser beam is aligned on the cantilever to give a zero signal from the PSPD i.e. the laser beam is reflected on to the center of the PSPD. Laser beam alignment is time consuming an improper alignment would cause change in force sensitivity of the system which in turn leads to false imaging [11].

d). Feedback controllers

To image the surface morphology, cantilever tip system is maintained to have a reference deflection or a reference height from the sample surface or the tip is excited at a certain frequency with a reference amplitude depending on the mode of operation utilized. This is called set point of the operation. During the scanning, there can be a change in the set point because of the surface features, which can be observed from the signal out of PSPD. The instantaneous values from the PSPD are compared with the reference values and the error signal between these two is minimized using proportional, integral and differential (PID) controllers. This error signal after the PID treatment is given to piezoelectric actuators which position the tip sample system. The purpose of the feedback controllers is to minimize the error signal to a small value as possible to maintain a reference deflection by the cantilever tip system throughout the measurement [11].

e). Data acquisition and Image display

The data acquisition and image display correspond to the image formation of surface morphology. The AFM manufactures provide a computer with a software through which the instrument is interfaced. Using the software we can also adjust the tip moment minutely which can't be done manually. Image processing and analysis will be done by using the software. During the scanning, we can also adjust the image acquisition time by changing the scan rate and the number of scan lines. But changing of scan rate of number of scan lines can compromise the image resolution [11].

3.4.4 Modes of operation in AFM

There are numerous imaging modes available for AFM, which include three main primary modes and several secondary modes. The modes of operation in AFM are explained by the distance regimes that they are operated in. The interaction force between the tip and the sample with respect to the separation distance is explained by Lennard-Jones potential [13].

$$F(r) = k\left[-\left[\frac{\sigma}{r}\right]^2 + \frac{1}{30}\left[\frac{\sigma}{r}\right]^8\right] \quad \ldots\ldots \quad 3.4.4.1$$

Depending on the force regimes, the AFM is operated in different modes. Below schematic gives the typical force regimes, under which AFM is operated.

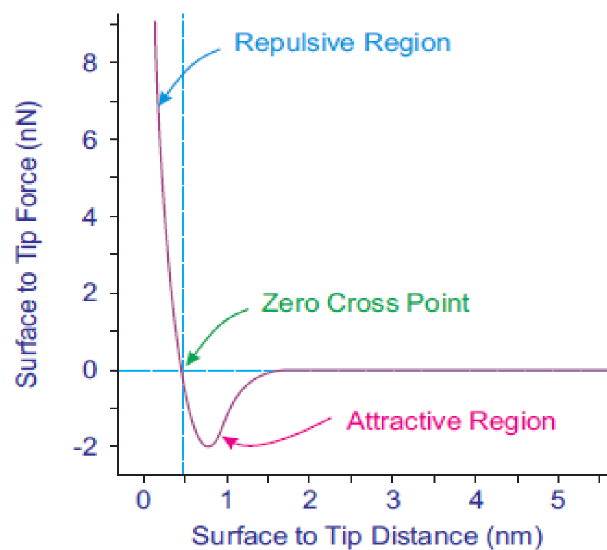

Fig 3.5.4.1: The schematic illustrating the distance regimes under which each of common AFM modes are operated. Image is reproduced from reference [14].

On the right of the above curve, the tip and sample are separated by large distance which causes no force on the tip. As the separation distance decreases the tip is attracted towards the sample. The more the separation decreases, the tip experiences a snap in and comes in contact with the sample and the distance lesser to this causes a repulse force on the tip and tip retracts away from the sample. A large contact force is experienced by the sample from the tip. If we increase the separation distance from this point, same curve is followed. There are three primary modes of operation: contact mode, intermittent contact or tapping mode and non-contact mode [15].

a). Contact mode

In the contact mode imaging, the probe remains in contact with the sample throughout the scanning. The interaction force between the tip and the sample lies in repulsive force regime with the tip-sample separation is less than 0.5 nm. There are two operating techniques in contact mode imaging: constant height mode and constant force mode. In the constant height mode, the tip and sample separation distance is kept constant and the feedback mechanism is switched off. The deflection of the tip when it scans the surface is recorded to give the topography of the surface. In the constant force mode, the force between the tip and the sample is kept constant by maintaining a reference deflection of the tip throughout the scanning utilizing the feedback controller. The difference in height during the scanning to maintain the constant force is recorded will give the topography of the surface. Deflection error signal is also recorded besides the topographic image, which stands as the replica of the topographic image. Constant height mode is used for smooth samples and low surface features. Contact mode operation is applicable for hard samples with relatively flat surfaces, since the tip in contact with the sample can scratch or deform the sample surface and the tip may be contaminated which lead to false imaging. Lateral forces also act when the tip traverses steep edges which can result a damaged tip and limits the resolution of the image. This can be overcome in tapping and non-contact modes [15].

b). Tapping mode

In tapping mode, the tip-sample interaction force lies in the attractive force regime with the tip-sample separation is greater than 0.5 nm. In the tapping mode, the tip above the surface is allowed to oscillate at a frequency close to its resonance frequency and maintained to have a characteristic amplitude called set point. But during the scanning, the change in the set point occurs as the tip engages and disengages away from the sample

because of the surface modulations. The feedback controller comes into action to correct the amplitude of the cantilever by changing its height by the use of z-piezo actuator. The change in height is recorded to construct the surface topography. During the scanning, there is a change in cantilever's frequency because of the amplitude change which causes a phase shift between the cantilever drive frequency and the actual frequency of the cantilever oscillating. This phase shift is recorded to construct phase image of the sample surface. Phase images describe the material properties of the surface such as friction, adhesion and viscoelasticity. In the tapping mode, tip oscillates above the sample surface, tip will exert less forces on the sample compared to contact mode. So, the tip life is more compared to contact mode with less sample and tip contamination. Lateral forces are minimized on the tip in tapping mode [15].

c). Non-contact mode

Similar to tapping mode, non-contact mode is operated in the attractive force regime. In non-contact mode, tip is excited to oscillate at a frequency as in tapping mode but with small amplitude. Feedback loop monitors the changes in amplitude during the scanning and sets a reference amplitude. The change in amplitude due to long range vanderwall and electrostatic forces between the tip and the sample is recorded to construct the topography of the surface [15].

3.4.5 Conductive atomic force microscope (C-AFM)

Conductive atomic force microscope (C-AFM) is the secondary imaging mode of AFM operated in contact mode and measures the conductivity of the samples. C-AFM characterizes the samples of conductivity variations on the surface by constructing a current contrast image [16]. This can measure the current ranging from pA to µA. The operation of C-AFM is explained by the below schematic.

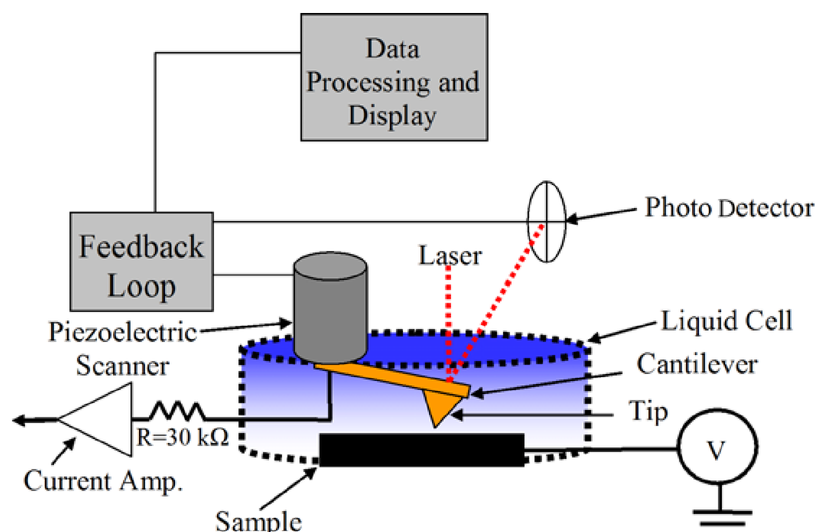

Fig 3.4.5.1: The schematic of principle of operation of C-AFM performed in a liquid cell. Image is reproduced from reference [17].

Typically the tips used in C-AFM are conductive. A DC bias voltage is applied between the tip and the sample which results in a current flow between them. A high current amplifier is connected in series with the probe which amplifies the current and constructs the current mapping image. During the scanning, feedback control which corrects the error signal works to maintain a reference deflection, constructs the topography of the surface as formed in contact mode AFM. Besides the topography, C-AFM is performed in spectroscopy mode, where the tip and the sample are kept stationery and a ramp voltage is being swept between the tip and the sample which gives the I-V characteristics of the sample at a local region. Using the spectroscopy mode, local electrical characterization is performed at nano scale equal to the tip dimensions [17].

3.4.6 Laboratory Instrument – Multimode8 SPM

In the present study for characterizing our phase change thin films, we used multimode SPM (MM-SPM). Multimode is designed for imaging the samples of maximum of 15mm*15mm dimensions. The sample is mounted on a metallic disk which is magnetically mounted on the sample holder. In MM-SPM, the tip is stationery and the sample moves back and forth using the piezoelectric scanner beneath the probe. For scanning, there are different scanners available with MM-SPM. They are as followed: J-scanners (AS-130VLR) offer a wide area scan of 125 µm × 125 µm with a vertical range of 5 µm, E-scanners (AS-12VLR) offer a scan area of 10 µm × 10 µm with a vertical range of

2.5 μm and A-scanners (AS-0.5) offer a scan area of 0.4 μm × 0.4 μm with a vertical range of 0.4 μm.

The total SPM set up includes an STM and an AFM with contact mode and tapping mode opertion utilizing feedback control system, input and display devices (Monitor, keyboard and mouse) and Nanoscope V controller. Computer (Monitor, keyboard and mouse) is used to interface the instrument using Nanoscope 8.10 software, through which instrument can be operated. Nanoscope V controller deals with the microscope stage which include sample motion unit (Piezoelectric scanner) and the detection unit (Laser and PSPD). The schematic of Multimode8 AFM is given in the figure 3.4.6.1.

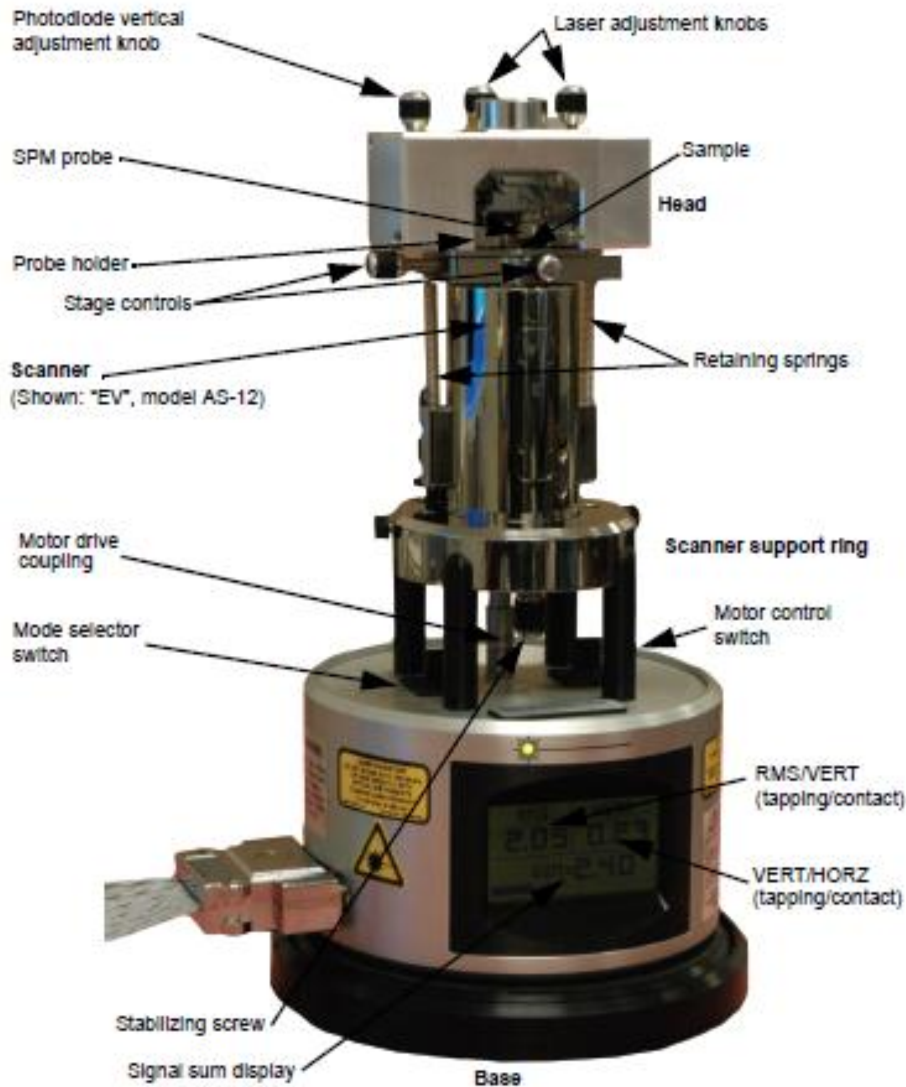

Fig 3.4.6.1: Schematic illustrates the instrument Multimode8 SPM. Image is reproduced from reference [18].

In the present study, we operated AFM in conductive mode. The scanner used for scanning the samples is J-scanner. A maximum of dc bias voltage of 10 V and ramping voltage of ±10V are approachable in C-AFM operation to study the electrical properties. The detectable current utilizing the module is in the range from few pA to μA. The tip specifications used for C-AFM operation is given in the table below.

Table 3.4.6.1: The tip specifications used for C-AFM opertion

Tip material	Sb doped Si
Cantilever thickness	1.5 – 2.5 μm
Cantilever length	405 – 495 μm
Cantilever width	45 – 55 μm
Resonance frequency	10 – 16 KHz
Force constant	0.2 N/m
Conductive coating on tip	20 nm Pt/Ir

For the present investigations to study the morphology and local electrical parameters, scan parameters maintained are: a) Scan rate – 0.5 Hz to 2 Hz b) Integral gain - 10, Proportion gain - 20. C) Deflection set point in C-AFM - 0.5 V.

References:

1. Glow discharge processes: plasma and sputtering: Edited by Brian chapman, Wiley, 1980.
2. Maissel, Leon I., and Reinhard Glang. "Handbook of thin film technology." New York: McGraw-Hill, 1970, edited by Maissel, Leon I.; Glang, Reinhard 1 (1970).
3. Severin, Kenneth P. Energy dispersive spectrometry of common rock forming minerals. Kluwer Academic Pub, 2004.
4. Zhou, Weilie, and Zhong Lin Wang. Scanning microscopy for nanotechnology: techniques and applications. Springerverlag New York, 2007..
5. Goldstein, Joseph, Dale E. Newbury, David C. Joy, Charles E. Lyman, Patrick Echlin, Eric Lifshin, Linda Sawyer, and Joseph R. Michael. Scanning electron microscopy and X-ray microanalysis. Springer, 2003.
6. Cullity, Bernard Dennis, and Stuart R. Stock. Elements of X-ray Diffraction. Vol. 3. Upper Saddle River, NJ: Prentice hall, 2001.

7. Pecharsky, Vitalij, and Peter Zavalij. Fundamentals of powder diffraction and structural characterization of materials. Vol. 69. Springer, 2008.
8. Waseda, Yoshio. Xray Diffraction Crystallography. Springerverlag Berlin Heidelberg, 2011.
9. Ferraro, John R. Introductory raman spectroscopy. Academic press, 2003.
10. Smith, Ewen, and Geoffrey Dent. Modern Raman spectroscopy: a practical approach. Wiley, 2005.
11. García, Ricardo. "Amplitude Modulation AFM in Liquid." Amplitude Modulation Atomic Force Microscopy (2010): 77-90.
12. Rugar, Daniel, and Paul Hansma. "Atomic force microscopy." Phys. Today 43, no. 10 (1990): 23-30.
13. Binnig, G., Ch Gerber, E. Stoll, T. R. Albrecht, and C. F. Quate. "Atomic resolution with atomic force microscope." Surface Science 189 (1987): 1-6.
14. Abramovitch, Daniel Y., Sean B. Andersson, Lucy Y. Pao, and Georg Schitter. "A tutorial on the mechanisms, dynamics, and control of atomic force microscopes." In American Control Conference, 2007. ACC'07, pp. 3488-3502. IEEE, 2007.
15. Bowen, W. Richard, and Nidal Hilal. Atomic Force Microscopy in Process Engineering: An Introduction to AFM for Improved Processes and Products. Butterworth-Heinemann, 2009.
16. Bhushan, Bharat. Scanning Probe Microscopy in Nanoscience and Nanotechnology 2. Vol. 2. Springerverlag Berlin Heidelberg, 2011.
17. Tomczak, Nikodem, and Kuan Eng Johnson Goh. Scanning probe microscopy. World Scientific Publishing Company, 2011.
18. Multimode8 with ScanAsyst instruction manual, Veeco instruments Inc. (2009, 2010).

Chapter 4

Results and Discussions

In this chapter, we discuss the results obtained from different characterization techniques utilized to understand the nature of the as-deposited thin films. The structural characterizations of $GeTe_6$ thin films have been investigated by X-ray diffraction (XRD) and Raman scattering studies. Compositional analysis of thin films was investigated by Energy dispersive X-ray spectroscopy (EDX) technique. The electrical properties of as-deposited thin films at nanoscale were studied using scanning probe microscope operated under conductive mode (C-AFM).

4.1 Compositional analysis by Energy dispersive X-ray spectroscopy (EDS)

Energy dispersive X-Ray spectroscopy is an analytical technique to measure the composition of bulk and thin films using X-ray emission due to the incident e-beam on the sample. It is mandatory to measure the compositional uniformity of thin films to confirm the homogeneity of the deposition, which in turn affects the electrical behavior of the thin film. In this study EDS analyses were carried out using our Scanning electron microscope (make: CARL-ZEISS).

In the present work, we analyzed the composition in nine different regions across the surface of the thin film. Fig.4.1.1 shows the schematic of sample geometry and R-1, R-2 and so on represents the regions of EDS measurements and the table explains the composition present in particular region corresponding to the ratio of Te to Ge. The measurement done in different regions explain that the compositional variation is in the acceptable limits. The ratio between the major components of Te to Ge is found to be $5.5 \pm \delta$, where δ value lies between 0 and 0.2. There were also the contributions to the composition from other components observed, which were found to be from the substrate and the electrode materials, since the depth of penetration for an EDS measurement is greater than 2 μm.

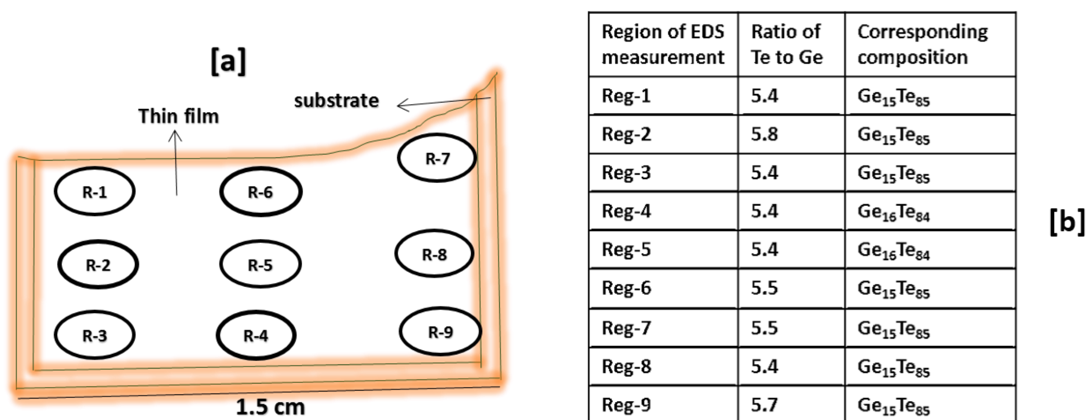

Region of EDS measurement	Ratio of Te to Ge	Corresponding composition
Reg-1	5.4	$Ge_{15}Te_{85}$
Reg-2	5.8	$Ge_{15}Te_{85}$
Reg-3	5.4	$Ge_{15}Te_{85}$
Reg-4	5.4	$Ge_{16}Te_{84}$
Reg-5	5.4	$Ge_{16}Te_{84}$
Reg-6	5.5	$Ge_{15}Te_{85}$
Reg-7	5.5	$Ge_{15}Te_{85}$
Reg-8	5.4	$Ge_{15}Te_{85}$
Reg-9	5.7	$Ge_{15}Te_{85}$

Fig 4.1.1: [a]. The schematic of the sample with different regions of EDS measurement. [b]. Table gives composition measured at certain regions. [c]. EDX spectrum obtained from a region.

So, the EDS measurement of amorphous thin films makes clear that the composition of the films is uniform throughout the film within the limits of the EDS measurements. Based on the confirmation from EDS studies, the sample will be referred as $Ge_{15}Te_{85}$ for the rest of the thesis.

4.2 Structural Characterization by X-Ray Diffraction

The structural characterization of amorphous thin films was analyzed using X-ray powder diffractometer (Panalytical X'pert pro diffractometer). The as-deposited thin films prepared by dc magnetron sputtering method are expected to be in amorphous state. Since, the deposition was carried out on a substrate maintained at room temperature; the adatoms are expected to spend their energies on chemisorption and will not possess sufficient energy for crystallization. Thus, we expect an amorphous $Ge_{15}Te_{85}$ thin film on glass substrate. In order to confirm the crystalline nature of the films, X-ray powder diffractometer was utilized. The diffraction pattern was recorded over a glancing angle ranging between ~3˚ to 50˚ (i.e., 2θ ~ 5 – 100˚). Fig. 4.2.1 shows the XRD pattern of as-deposited thin films. Though, there were no distinct diffraction peaks observed in the XRD pattern, but pattern observed seems as if it had a peak possible at around 27˚ which can be seen for cubic Ge and Hexagonal Te. In order to clarify this, we have compared this pattern with the regular XRD pattern of glass slide. The XRD pattern obtained for $Ge_{15}Te_{85}$ thin films resemble the pattern obtained for the glass slide. The broad scattering peak at 27˚ obtained for $Ge_{15}Te_{85}$ thin film which can also be seen for glass slide confirms the amorphous nature of thin films. However, it is known that $Ge_{15}Te_{85}$ composition shows a dual stage amorphous to crystalline transformation with Te and GeTe crystallites formation at different temperatures [1] and it is

expected that Te tends to crystallize at room temperature as reported in literature [2]. Within the limits of X-ray powder diffraction it is evident that no such Te segregation in the form crystallization had occurred in the as deposited $Ge_{15}Te_{85}$ thin films at room temperature.

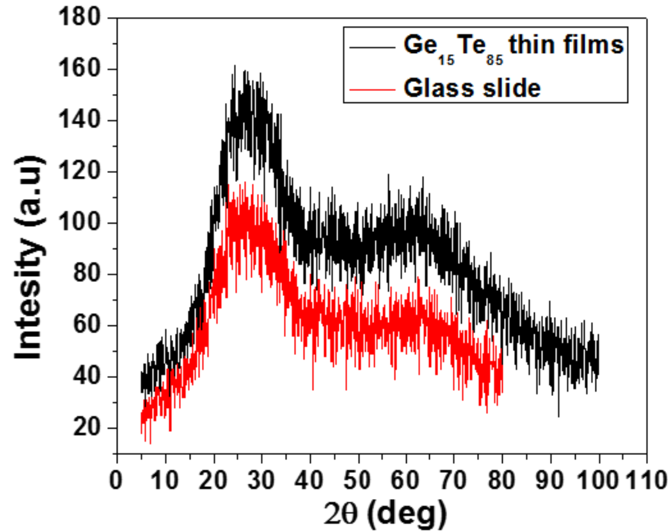

Fig 4.2.1: The XRD pattern of as-deposited $Ge_{15}Te_{85}$ thin films

4.3 Raman Spectroscopy studies of $Ge_{15}Te_{85}$ thin films

Raman spectroscopy is the technique to investigate the local vibrational modes present and gives the details of any changes that involve structural modifications. Especially phase change memory (PCM) materials experience changes in local atomic arrangement during amorphous to crystalline transformation. Hence, Raman scattering studies are advantageous to analyze remarkable difference between the local atomic arrangements in both the amorphous and crystalline phases.

In our present work, room temperature Raman scattering studies were performed using Senterra Raman spectrometer (make: Bruker). The Raman scattering studies were done on amorphous thin films with low powers of 10mW with an integration time of 10 seconds and with a laser wave length of 785 nm. The resolution of the data obtained from Raman pattern is 3 cm^{-1}. Fig.4.2 shows the Raman scattering study of amorphous thin films. The Ge-Ge bonds are ruled out in Te-rich amorphous GeTe system which was proven by the Raman scattering measurements [3, 4]. Raman bands were seen at 125 cm^{-1} and 143 cm^{-1}, which could be attributed to Ge-Te bonds. Raman shift at 143 cm^{-1} is looking stronger due to the shoulder present at ~155 cm^{-1}, which could be attributed Te-Te bond. This suggests that there is a plausible mixed co-ordination present in the sputter deposited $Ge_{15}Te_{85}$ thin

films. There were no bands observed related to Ge-Ge bond, which can be seen for Ge-enriched glasses at 275 cm^{-1} for Ge-Ge vibrational mode [4]. Hence, presence of any self co-ordinated Ge can be ruled out when we consider amorphous $Ge_{15}Te_{85}$ thin films.

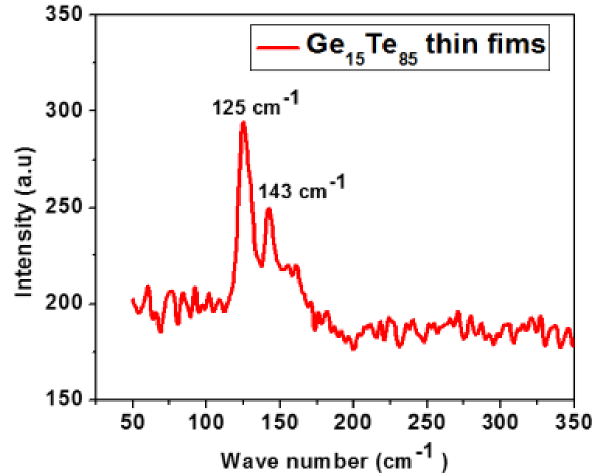

Fig 4.3.1: Raman Spectroscopy of amorphous $Ge_{15}Te_{85}$ thin films

As explained in the literature, in the amorphous structure of $Ge_{15}Te_{85}$ each Ge is coordinated by four Te atoms and each Te has no Ge neighbor in their first coordination sphere and it is described by $GeTe_4$ tetrahedra as structural units which are bridged via Te-Te bonds [5]

4.4 Electrical property studies of highly oriented pyrolytic graphite (HOPG) using C-AFM

The conductive atomic force microscope is the secondary imaging mode derived from contact mode AFM. In C-AFM, a dc bias is applied across the sample and the probe which is conductive. With the application of dc bias voltage, there is a current between the tip and the sample, which is obtained as a current mapping image along with the regular contact mode topography of the scanned area. In the present study, we employed different biasing voltages to measure the local electrical properties of thin films to investigate the threshold switching and memory switching behavior of thin films. The present studies were carried out using the instrument "Make: Multimode8 – Bruker". The AFM images were processed and analyzed by Nanoscope analysis software.

Before we start to perform on as-deposited thin films, we performed C-AFM operation on the standard pristine sample of "highly oriented pyrolytic graphite" (HOPG) supplied by Bruker to calibrate the instrument.

HOPG is used as a standard specimen for Scanning tunneling microscope (STM) and AFM. HOPG is a special type of graphite prepared by exposing pyrolytic graphite which is formed from the decomposition of hydrocarbon gases on a heated surface to high pressure and temperature with high annealing times. HOPG has a lamellar arrangement of identically stacked two dimensional graphene sheets along the c-axis. This lamellar arrangement of ABAB… stacking is ordered over short distances and there is a rotational disorder (i.e. angular misorientation or mosaicity) between the graphene layers. Depending on high pressure and temperature, one can get HOPG materials with different mosaic spreads. Each two dimensional graphene sheet consists of hexagonal lattice of carbon atoms bonded by sp^2 hybridization. There is a weak Vanderwall interaction between the graphene layers through the π orbital electrons and this π orbital electrons along the c-axis are responsible for the conduction along the basal plane. Because of this weak vanderwall interactions, graphene layers slide against each other and can be peeled off easily. In the basal plane each carbon is strongly bonded with three other carbons and the distance between neighboring carbon atoms is 1.42 A° [6, 7].

Because of the extended π electrons, HOPG exhibits the anisotropy electronically by showing a metallic behavior along a-axis and semiconducting to semi metallic behavior along the c-axis. The electrical conductivity along the a-axis is the order of 10^5 $(\Omega\text{- cm})^{-1}$ and 10^3 $(\Omega\text{-cm})^{-1}$ along the c-axis. There are two different edge states present in graphene sheets which will influence the π electronic states, they are: (1) arm chair (cis) and (2) zigzag (Trans) edges. The edge states in zigzag edges are localized with high electron density compared to armchair which don't have any edge states making them less conductive than zigzag edges. Fig 4.4.1. shows the schematic illustration of different edge states present in graphene sheets.

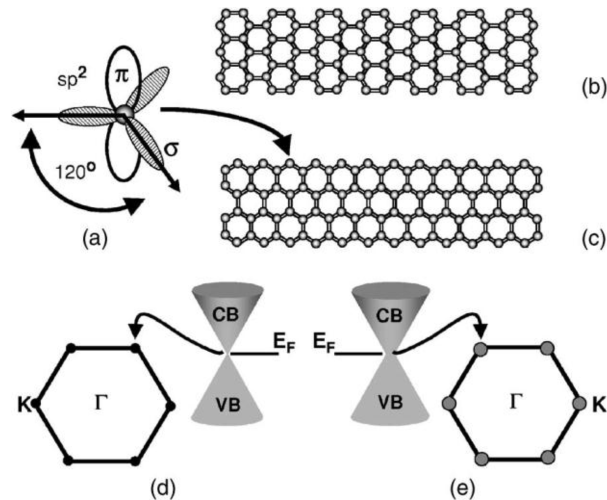

Fig 4.4.1.: (a) Carbon atoms showing sp^2 hybridized σ orbitals in the a-b plane and nonhybridized π orbitals along the c axis of the graphite layer. Graphite sheet/ribbons showing arm chair (cis) edge and (c) zigzag (Trans) edge. (d) Six points in the Brillouin zone showing zero gap and having zero overlap of the conduction band and valence band at Fermi energy (E_F), i.e., zero density of states (DOS) at Fermi energy and (e) finite overlap of CB and VB leading to finite DOS at E_F. Image reproduced from the ref [7].

When we peel off the top layer of HOPG to remove the surface contamination, they will be peeled off inhomogeneously. Because of this, there is also a slight dislocation of the layers and they will be crumpled. The top layers which are loosely held with the beneath always show higher conductance than the lower and there is a dip in the current in the lower layers because of the depletion of the local electron density [7]. The crumpling of the layers also induces displacement of carbon atoms in and out of the plane. The valence and conduction band of six isolated atoms in the Brillouin zone of hexagonal lattice overlap for nearest neighbor hopping of π electrons which are induced by the distortions of carbon atoms introduced by the crumpling. This can lead to an increase in conductivity [7].

Study of electrical properties of HOPG using C-AFM

To calibrate the instrument for C-AFM operation, HOPG samples, supplied by Brukers are of 12 mm x 12 mm mounted on a steel disc. The magnetic chuck sample holder mechanism enables HOPG sample to mount on it. The probe used is a Sb doped Si with Pt-Ir coating for conductivity measurements and the spring constant of the cantilever is about 0.2 N/m. The initial tip radius of curvature is about 20 nm. The scanner used for imaging is AS-130 VLR scanner (with 125 μm x 125 μm XY range and 5μm Z range). The conductive tip scans the selected area in contact mode with a biasing voltage applied to both the tip and the sample and generates the current mapping image along with the topography. Before start to proceed for the C-AFM operation, the surface of HOPG sample is exfoliated manually using the scotch tape to remove the surface oxidation.

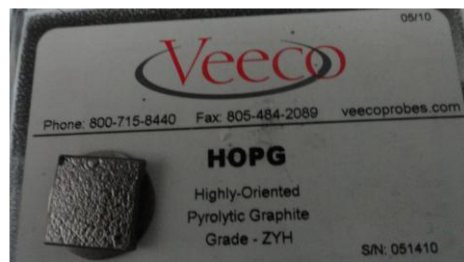

Fig 4.4.2: Geometry of calibrating specimen for C-AFM studies. Pristine sample of HOPG.

Fig 4.4.2 shows the sample geometry of HOPG used for calibrating the instrument for C-AFM operation. After the sample is mounted on the sample holder and setting up parameters of C-AFM operation, tip is made engaged to contact sample. After the tip engaged, we scanned the sample in large areas under zero bias condition to understand the roughness of surface. We didn't scan the sample in small areas, since the sample roughness is too high to probe the features of the surface intricately, which can mislead us to false interpretation. Though the large scan gives good imaging, but the spatial resolution of the image will be lost compared to small scan sizes.

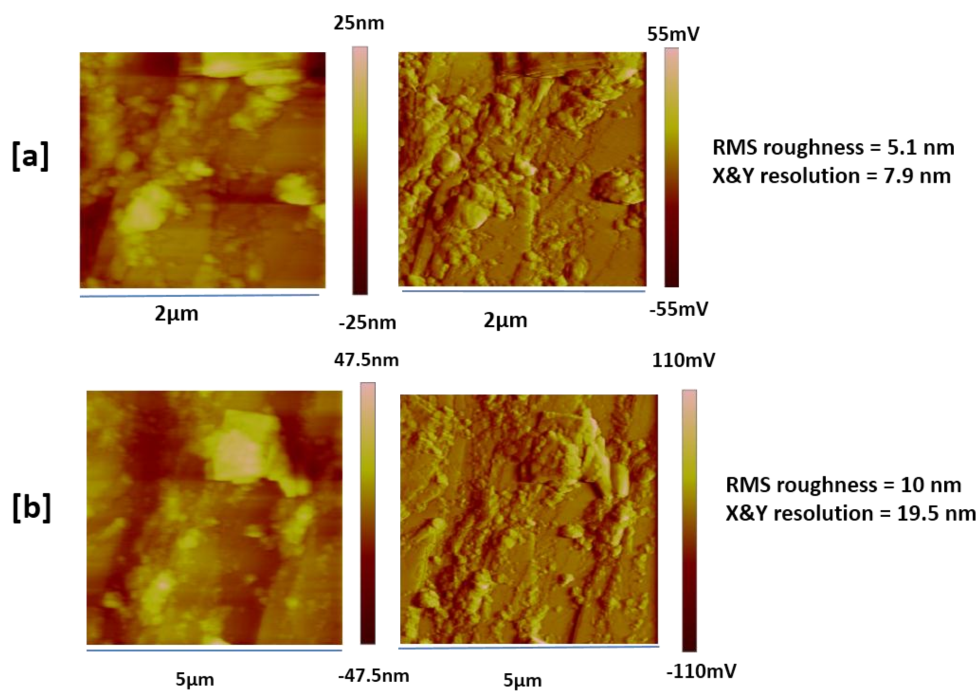

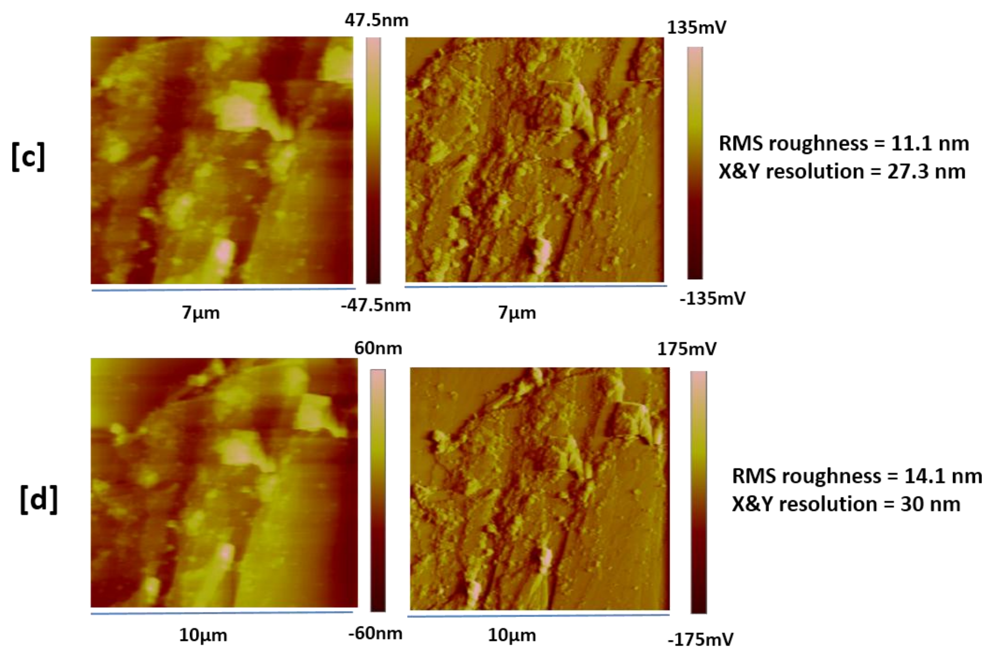

Fig 4.4.3: [a], [b], [c] and [d] show the topography and deflection error images of HOPG with zero bias voltages in scan regions of 2 µm, 5 µm, 7 µm and 10 µm respectively.

Fig 4.4.3 shows the topography and deflection error image of HOPG samples generated by scanning in various scan areas of 2 x 2 µm. 5 x 5 µm, 7 x 7 µm and 10 x 10 µm. All these scans were performed under zero bias conditions to observe the surface of HOPG. The deflection error image shows how the instrument would construct the topography utilizing the change in deflection when the tip traverses on the sample. It can be considered as the replica of actual topography of the sample. From the observations of the roughness data, it is clear that sample surface is so rough and the RMS roughness is mentioned with the images. Since the manual exfoliation is performed in an uncontrollable fashion, few layers were torn off and few layers were crumpled and some of them were twisted, giving rise to an irregular surface. All the scans were done in large area, because of highly rough sample surfaces which can break the tip when they are scanned in low scan areas.

To understand the electrical properties of HOPG, bias voltages of 0.5 V and 1 V were applied to observe the current mapping images comparing them with the topography.

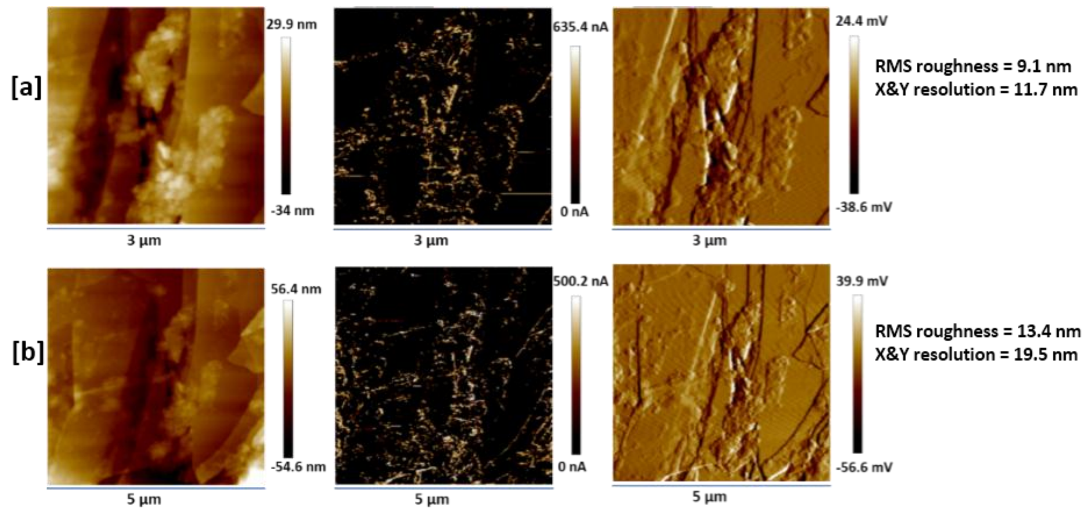

Fig 4.4.4: [a] & [b] show topography (left), current mapping (middle) and deflection error (right) images obtained with a biasing voltage of 0.5 V in scan regions of 3 µm and 5 µm respectively.

Above images (middle) show the current mapping of HOPG sample with the application of a bias voltage of 0.5 V in an area of 3 x 3 µm and 5 x 5 µm. The current mapping image clearly depicts sample surface features and in fact it clearly reveals the surface roughness showing different current contrast as seen in figure 4.4.4. We couldn't get a clear current mapping image, which is limited by the spatial resolution of AFM when performed in large scan areas and relatively rough surface of HOPG. Current features were not alleviated properly, but the current mapping image is showing distinct edges of layers by showing a current contrast. We have drawn the line profile for 3x3 µm scan area to understand the current features with the modulations in the surface topography. Figure 4.4.5 shows the line profiles drawn for both the topography and current mapping images.

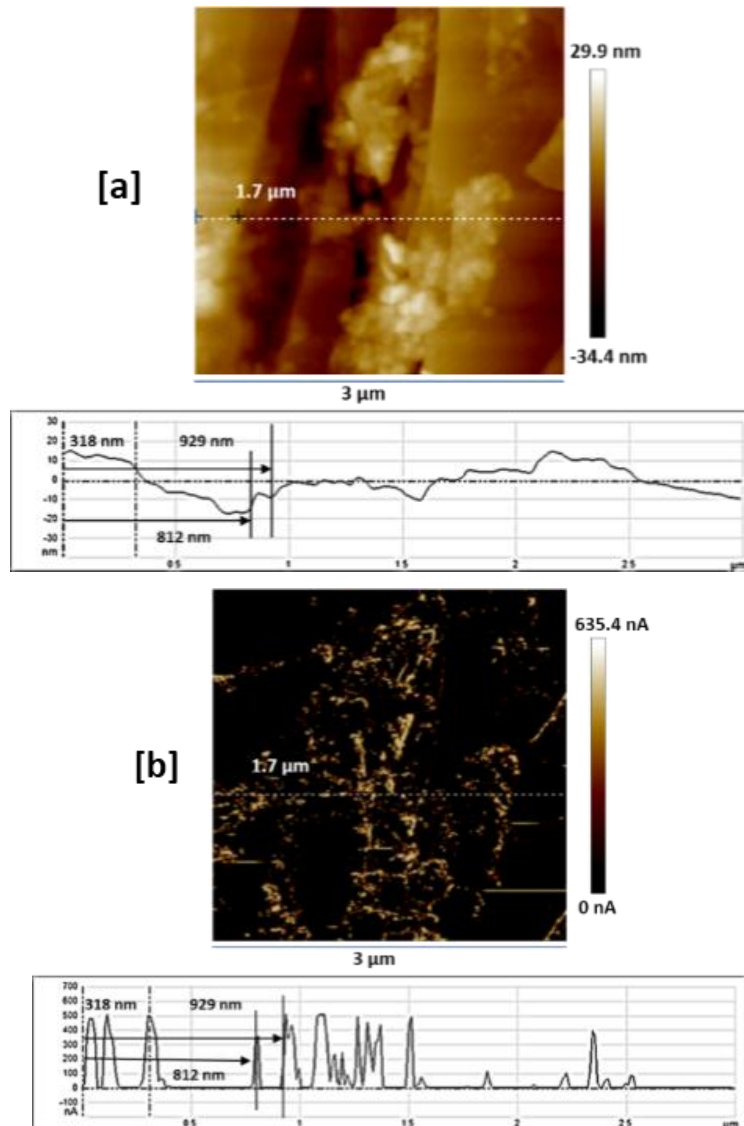

Fig 4.4.5: [a] and [b] images on the top and the bottom show the line profile data for a sectioned line at 1.7 µm from the top for both the topography and current mapping images.

From the line profiles depicted in the figure 4.4.5, it can be understood that we sectioned both the current mapping and topography images in the same region so that we can correlate the current features with the modulations in the topography. If we observe the line profiles with their corresponding current mapping and topography images, we can make out that at 318 nm away from zero point there is a gradual dip in the topography which was observed by the dip in the current at the same point. If we move further to 812 nm, there is a small and sudden increase in the current which could be seen in the topography as a sudden change to upper layers which could be understood as there is a sudden increase in the current at the interface of step edges of lower and upper layers. At 929 nm away from zero

point, there is again a change to upper layer which can be realized by sudden increase in current. It is also clear that we can observe the current features at step edges separating two different layers.

The current contrast in HOPG is also verified using the I-V characteristics in C-AFM operation. In the I-V spectroscopy mode, the tip will be in contact with sample and a voltage ramp is applied to the tip and the sample to generate I-V characteristics at that particular point or the tip contact region. To switch from scan mode to ramp mode, the tip should at least scan some area in its regular scan mode, after which ramp mode can be initiated and the ramping is performed in the scanned region by selecting the point of ramping. To measure the I-V characteristics, we chose a 5 x 5 μm region in which we selected two random points where the tip also measures the current from that point on the surface. The figure 4.4.6 given below shows the scanned region along with the points of ramping where the I-V characteristics were measured.

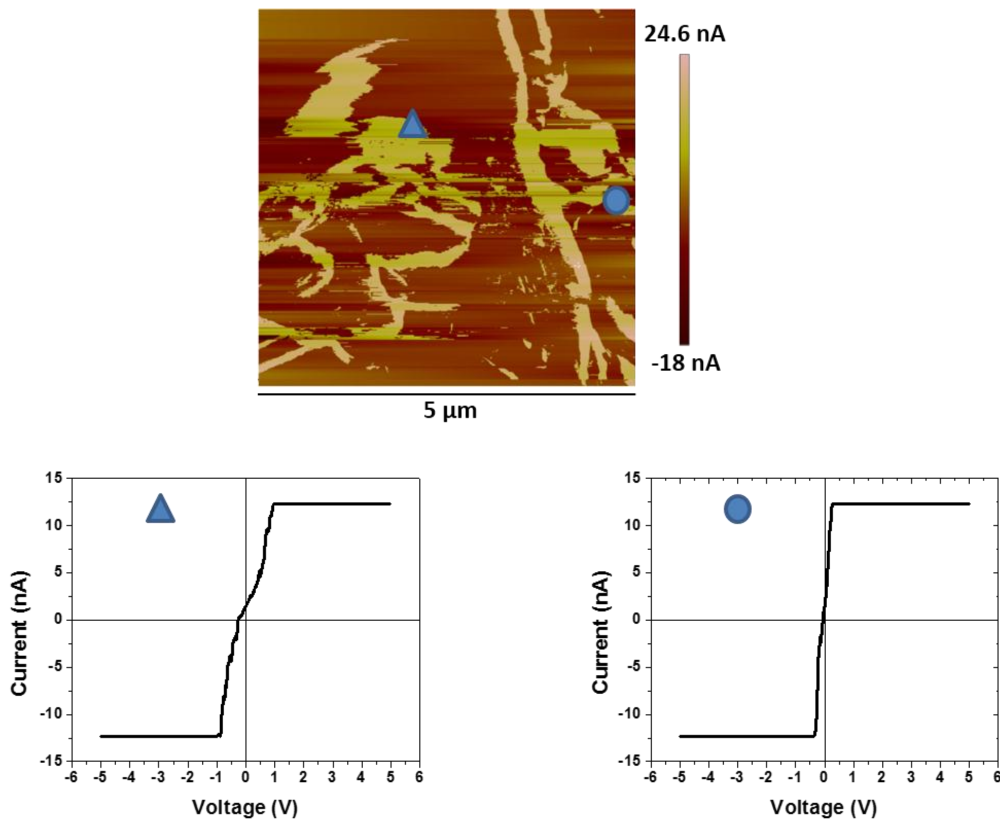

Fig 4.4.6: [a]. The current mapping image of 5 μm region before switched to ramp mode. [b] And [c] give the I-V characteristics of the points (triangle and circle) selected in a 5 μm region.

The figure 4.4.6 clearly reveals that there is a current contrast in the conductivity mapping obtained from HOPG. The selected points where the I-V curves were recorded are represented by a triangle and a circle. I-V characteristics obtained from both triangle and circle points, show similar I-V characteristics, with minor change in the magnitude of current for the given applied voltage, which is also in accordance with the current mapping. Thus, the conductivity mapping and I-V measurement from a given point on the sample was performed successfully on HOPG samples. The obtained results were compared with the existing literature [7] and found a good correlation with our studies. On optimizing the scan parameters and the transport parameters, we further proceeded with the electrical studies of $Ge_{15}Te_{85}$ thin films.

4.5 Electrical Characterization Of Amorphous $Ge_{15}Te_{85}$ thin Films Using C-AFM

As detailed earlier, phase change memory materials undergo a phase transition from its amorphous state to crystalline state with the application of electrical field. Since, the motive of our project is to study the electrical properties associated with the phase change, we characterized our amorphous thin films using C-AFM to investigate the nanoscale electrical properties.

4.5.1 Morphology of amorphous thin films

The samples were mounted on a steel puck using a silver paste for electrode purpose. As the thin films were deposited on glass substrates which undergo C-AFM characterization, it requires a conductive channel unto the thin film from the electrode. So, a thin conductive channel is made between the thin film surface and the steel puck using the silver paint. And then we left our sample for 1hr to cure and to ensure the intimate contact between the film and the puck. Figure 4.5.1.1 shows the schematic of the samples that were subjected to scanning probe studies. All our samples were prepared in similar manner before performing scanning probe studies.

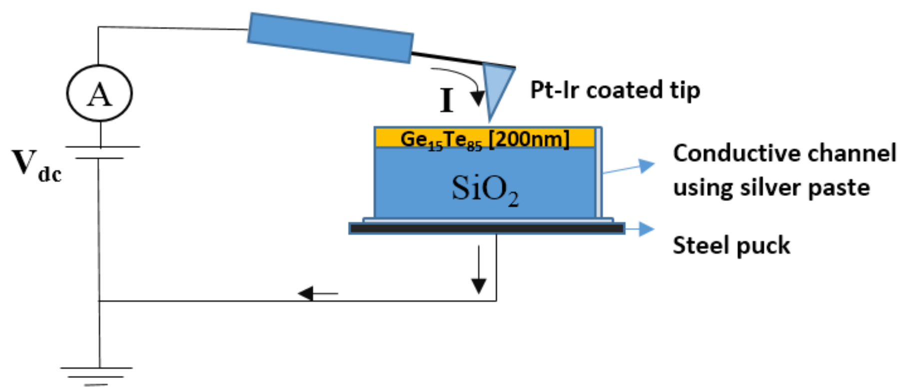

Fig 4.5.1.1: The experimental set up depicting the C-AFM measurements.

The region to be scanned on the sample was selected using the optical microscope equipped with the AFM and the automatic measurements were made with the optimized scanning parameters followed for the standard specimen (HOPG) to obtain best possible outcome. The C-AFM module used in our experiment can measure currents up to maximum of 1 μA with the lowest of few pA. Nanoscope analysis software is used to analyze the AFM images. As we already confirmed that the thin films are in pure amorphous nature using XRD and Raman scattering studies, we planned to study the phase change behavior with different voltages. For morphology, we imaged in different regions with different scan areas. In the present chapter, we performed measurements on four different scan sizes and is shown in the figure 4.5.1.2.

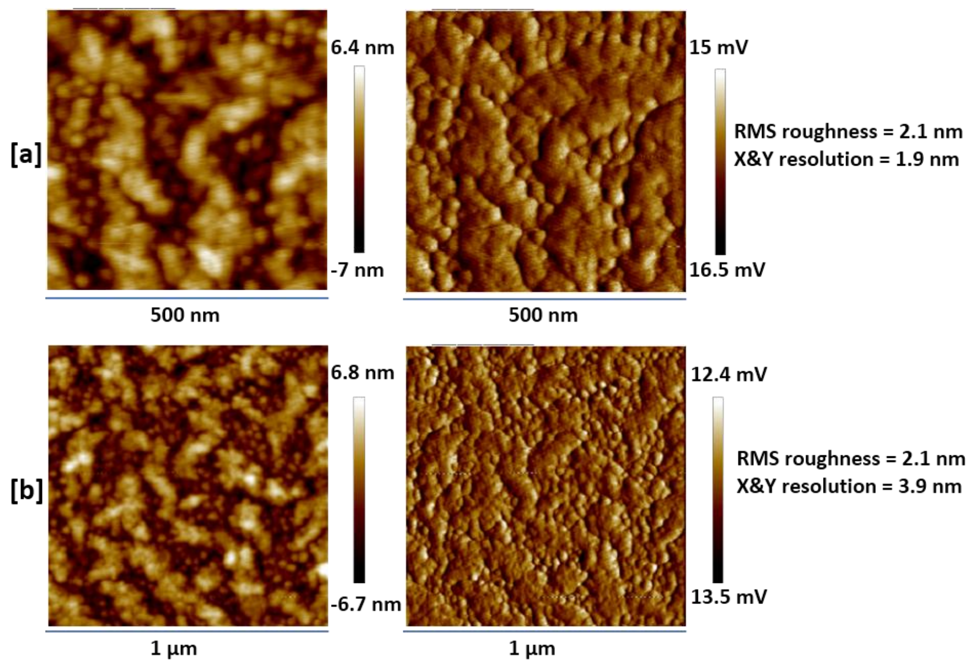

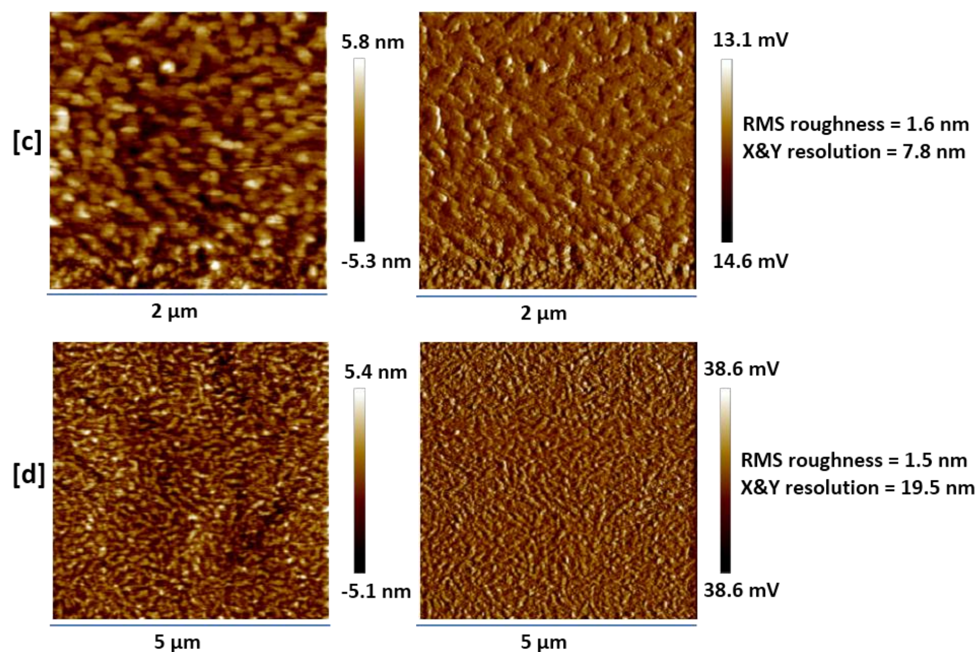

Fig 4.5.1.2: [a], [b], [c] and [d] show the topography and deflection error images obtained in 500 nm, 1 µm, 2 µm and 5 µm respectively.

Above figure 4.5.2 depicts the morphology and corresponding deflection error images measured with different scan sizes. Measurement parameters including the resolution of the images are mentioned in the image itself. Morphological studies were performed by applying biasing voltages less than 1.5 V. The voltages used to investigate the morphology were carefully chosen such that they are less than the threshold switching voltage of $Ge_{15}Te_{85}$. Hence, there would not be any phase change induced in the film due to the scan performed. If any phase change was induced it is expected to drive some changes such as volume, density, roughness and etc on sample. The lower scan sizes such as 500 x 500 nm and 1 x 1 µm are always preferable to acquire the best resolution of the image to understand the surface features in the nano regions. The rms roughness of the films observed with different scan sizes is in the range between 1 nm and 2 nm. The deflection error image is more of a replica of topographic image clearly showing the distinct features of the surface rather than we could see in topographic image. The higher scan size images such as 2 x 2 µm and 5 x 5 µm are useful to study the steps present in the sample. But from the morphological observation, it is made clear that the roughness values associated with different scan sizes are almost equal. There is no deviation observed in the surface modulations when we compare both smaller and large area scans. The current mapping images for the above scans were not included in the above figure, because the current shown up in current mapping images is almost negligible (voltage lower than threshold switching)

and far below the instrument limit which shows a current of ~3 pA. From these observations, it is also understood that thin films are highly resistive to respond to the applied biasing voltages less than 1.5 V. So, the morphological observations with measured roughness values explain that thin films are relatively smooth and they are at high resistance state, i.e. amorphous state.

4.5.2 I-V characteristics of amorphous thin films

For a phase change material, threshold switching is the voltage which transforms the material from high resistive to low resistive state. If the material undergoes a resistive change associated with structural transformation like amorphous to crystalline, it is called as **memory switching** [8] and if there would not be any structural change but only resistive change exhibited, it is called as **ovonic threshold switching** [8]. I-V characteristics performed on thin films have shown the switching behavior of amorphous films when the voltage exceeds the threshold value. The variation in the threshold switching values was observed by performing the I-V characteristics at different positions in a 500 x 500 nm region. These measurements were performed with a ramp rate of 0.5 Hz and the delay time between the data points is ~2 ms.

In the preliminary investigations to measure I-V characteristics, we applied low ramping voltages of 0 to 3 V to characterize the threshold switching behavior of amorphous phase change thin films of $Ge_{15}Te_{85}$. Figure 4.5.2.1 (a) shows a typical I-V curve obtained from $Ge_{15}Te_{85}$ thin films, which is in accordance with the expected behavior from any phase change material.

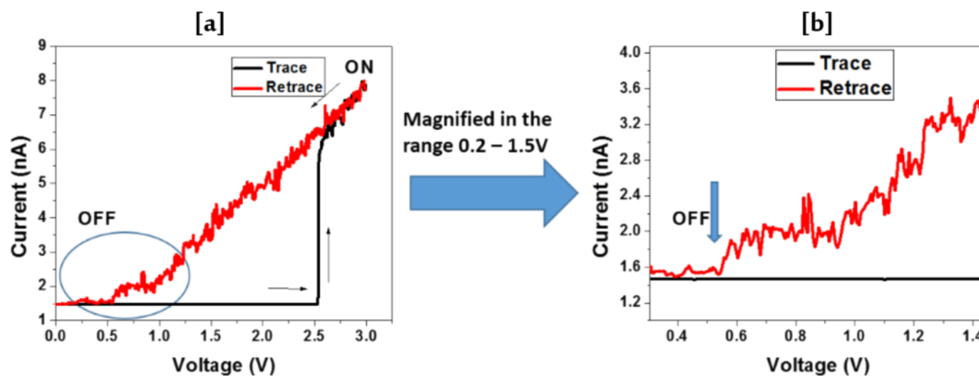

Figure 4.5.2.1 – [a] A typical I-V curve obtained from $Ge_{15}Te_{85}$ thin film exhibiting phase change characteristics, [b] Magnified I-V curve in the range of 0.2 to 1.5 V.

I-V ramps were performed in a selected 500 x 500 nm region which is scanned with zero biasing voltage. We have randomly selected 48 points in the 500 x 500 nm regions. If we observe the trace and the retrace path of the I-V curve shown in figure 4.6.2.1, it describes that when the voltage reaches a value of 2.5 V, the amorphous films are switched to a high conductance state. Though the behavior is as expected, it does not confirm that there is a complete amorphous to crystalline transformation in the sample. In order to further verify the same we observed the retrace curve shown in the enlarged image of figure 4.5.2.1[b] (right). In the retrace curve, the current is reaching zero at a non-zero voltage by leaving the material again in to high resistive state. Hence, the sample has not undergone a permanent structural change from amorphous to crystalline at the probe point, however it is evident that it has undergone a resistive change. Hence, the ON and OFF states mentioned in the above curve represents the amorphous resistive and amorphous conductive states.

In the retrace curve in the figure, the non-zero voltage where current reaches a zero value is called as the holding voltage [8] of the films. Since the switching is not involved with any structural transformation, it is called ovonic threshold switching. When the voltage reaches ovonic threshold switching, there is a breakdown of carriers and are emitted from the valence band and the trap states and they reach the conduction band states, which results in sudden increase in the current as explained in reference [9]. In addition it was confirmed by repeating the I-V curves in a given point without retracting the probe. Such repetition is expected to show no switching characteristics, if a memory switching associated with crystallinity had happened. Hence, the switching we had observed is mostly likely a resistive switching, with a word of caution that different pulse width were not employed for the set and reset observation. IV curves from different regions of the sample were also recorded and the summary of the results are given in figure 4.5.2.2

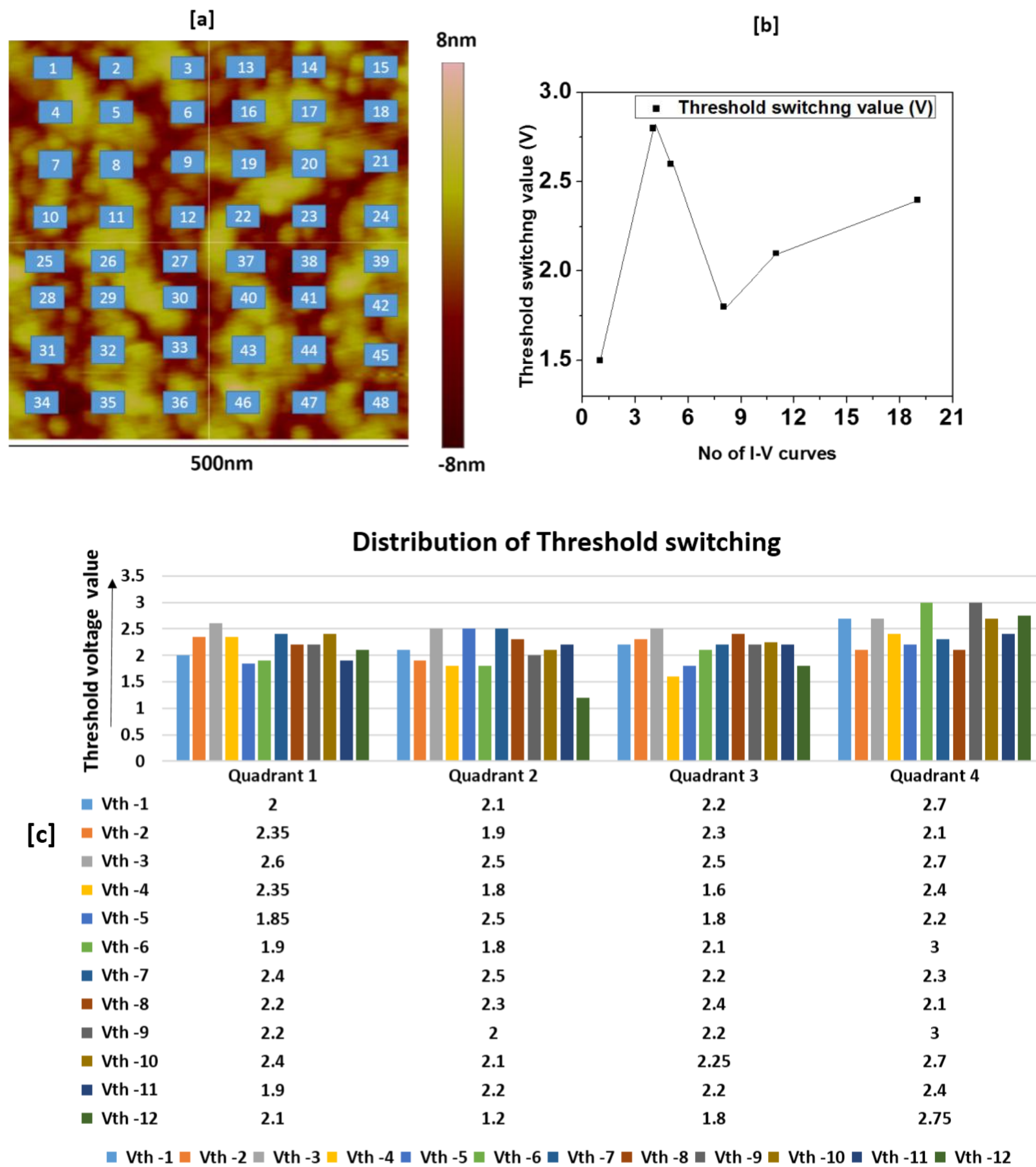

	Quadrant 1	Quadrant 2	Quadrant 3	Quadrant 4
Vth -1	2	2.1	2.2	2.7
Vth -2	2.35	1.9	2.3	2.1
Vth -3	2.6	2.5	2.5	2.7
Vth -4	2.35	1.8	1.6	2.4
Vth -5	1.85	2.5	1.8	2.2
Vth -6	1.9	1.8	2.1	3
Vth -7	2.4	2.5	2.2	2.3
Vth -8	2.2	2.3	2.4	2.1
Vth -9	2.2	2	2.2	3
Vth -10	2.4	2.1	2.25	2.7
Vth -11	1.9	2.2	2.2	2.4
Vth -12	2.1	1.2	1.8	2.75

Fig 4.5.2.2: [a]. I-V probes at different points in a 500 nm scanned region. [b]. No. of I-V curves showing similar threshold switching values. [c]. Distribution of threshold switching values over different probe points.

Figure4.5.2.2 [a] shows the schematic of the probe points in different quadrants of the selected 500 x 500 nm region, [b] shows the typical number of curves that exhibited certain threshold switching, [c] shows the distribution of threshold switching values observed in different quadrants. I-V characteristics were observed with ramping voltages of 0 to 3 V. From the fig [b], it is clear that most of I-V curves have shown a threshold

switching value of 2.2 V. In the above experiment, the threshold switching values for different probe points observed have a range in different points with most of I-V curves exhibiting a threshold switching voltage (V_{th}) value in between 2.2 and 2.4 V and there is a slight variation in holding voltage (V_h) observed. When amorphous conductive state is reached with the application of threshold field, this state can be retained even if we retrace back from threshold voltage and maintained till the holding voltage, which is equal to the optical band gap of its crystalline state, as reported in [8, 9]. The variation in V_h might be due to, the C-AFM measurements performed in planar configuration and we don't know the voltage drop at the electrodes and the voltage barrier formed with different probe points. I-V characteristics also explain that there is no memory switching in the probed region, since there is no crystallization affects observed in that region.

From the observations of I-V curves obtained from all the points with 0 to 3 V, it is made clear that all the I-V curves have shown a holding voltage which proves that there is no memory switching at any probe point. We have also cross checked the ovonic threshold switching behavior by scanning the same 500 x 500 nm region with low voltages less than 1.5 V (reading voltages) where I-V ramps were performed. The scanned image did not show up any crystalline spots which showed the lowest detectable currents as seen for amorphous thin films. From above experiment of I-V ramps at different points over a complete scanned region, it makes clear that the all the probe points suffered the ovonic threshold switching. The threshold switching values are almost uniform throughout region with minor variation in the holding voltages.

As explained earlier to observe the memory switching behavior through I-V characteristics, we performed multiple I-V ramps at a single probe point with ramping voltage higher than the earlier experiment. We tried to retrieve the memory switched region in a small area scan with low biasing voltages. But, we couldn't observe any such memory switched region in the scanned region. It is expected because of either the tip area was so small (20-30nm) to probe in the large area scan or the reason might be that when the tip traversed such a region if it did not probe that particular area, no current could be observed.

4.5.3 Memory switching of amorphous thin films

To understand the memory switching behavior of amorphous $Ge_{15}Te_{85}$ thin films, we have done a series of scans in such a way that first an amorphous region is made crystalline by applying a sufficient bias voltage and then the crystalline region is reproduced with relatively small bias voltage (read voltage) in a large amorphous region. The region which is made crystalline will show a current contrast with the surrounded amorphous region.

Before proceeding for memory switching experiment, we scanned a region with different scan sizes with zero biasing voltages so that this region can be realized when they suffer high voltages which can make them crystalline. When, we apply high biasing voltages to small scan areas, these high voltages can disturb the image quality and the morphological features will look noisy and sometimes they will be lost. So, before going to image a small area with high biasing voltages, it would be better to have certain small area scanned with zero biasing voltage. First of all we have scanned a 1 x 1 μm, 500 x 500 nm and 300 x 300 nm regions consecutively in a single region. After the 300 x 300 nm region is scanned with zero bias voltage, we scanned the same region with 2.5 V bias voltage to make it crystalline. And we wanted to realize the crystalline 300 x 300 nm region in a 1 x 1 μm region by applying relatively small voltages (aka read voltages).

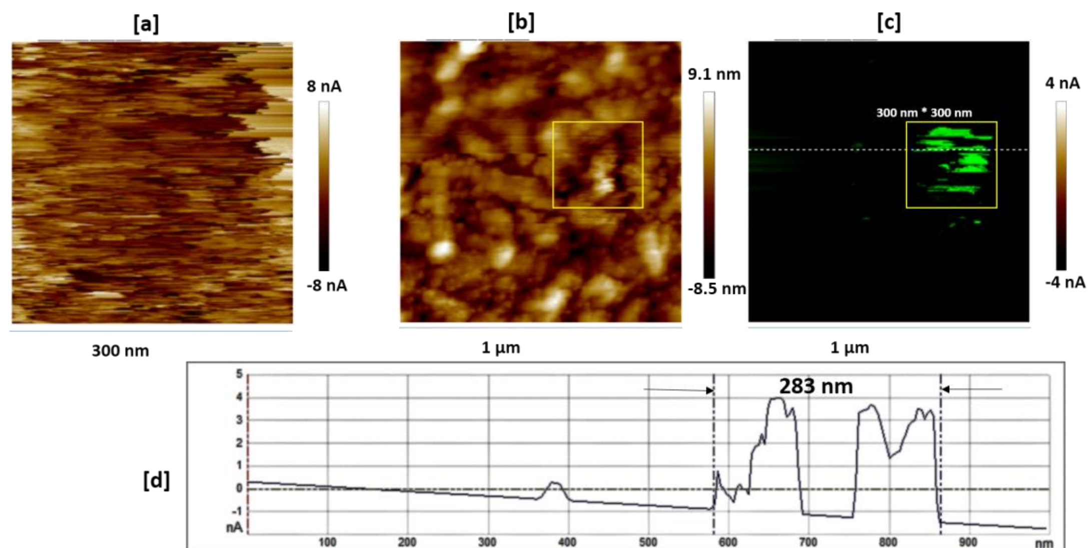

Fig 4.5.3.1: Current mapping image generated with an applied bias voltage of 2.5 V in a 300 nm region. [b] And [c] represent the morphology and corresponding current mapping image generated with 1 V bias voltage in a 1 μm region and [d] shows the sectioned image (Line profile) of current mapping at 384.4 nm from the top.

From the figure 4.5.3.1, it makes clear that the applied 2.5 V (equivalent to the threshold voltage) bias voltage induced the heating effects which made the whole 300 nm region conductive while performing the scan as shown in figure. The effect of it was observed in the next consecutive scan made in a 1μm region with low biasing voltage of 1 V. It is unambiguously evident that a conductive crystalline region of (300 x 300 nm) was observed and is shown with the yellow box in the morphological and current mapping image. In addition to this, the line profile which is drawn for the current mapping image also confirms the presence of high current in memory switched 300 x 300 nm region. Thus, the memory switching behavior indicates the transformation from amorphous to crystalline phase present in $Ge_{15}Te_{85}$ thin films. From the aforementioned observations, it is clear that the 2.5 V applied biasing voltages are sufficient to crystallize the thin films.

We have also cross checked memory switching by continuing similar experiments at different region and also at larger scan areas. After we read the crystalline 300 nm region in a 1 μm region, we have again scanned the 1 μm region with a bias voltage of 3 V to make it completely crystalline and then we reproduced the 1 μm crystalline region in a 3 μm scan region by applying the read voltages. Again another set of measurement is done by making this 3 μm region crystalline which was retrieved in a 10 μm scan with a read voltage. In these three set of measurements, we clearly observed that the regions we scanned with high biasing voltages (≥ 3 V) suffered the structural transformation and could be reproduced with low biasing read voltages. These three set of measurements were explained by the figure shown below.

[a]. Step 1: Imaging in a 1 μm scan area with a biasing voltage of 3 V

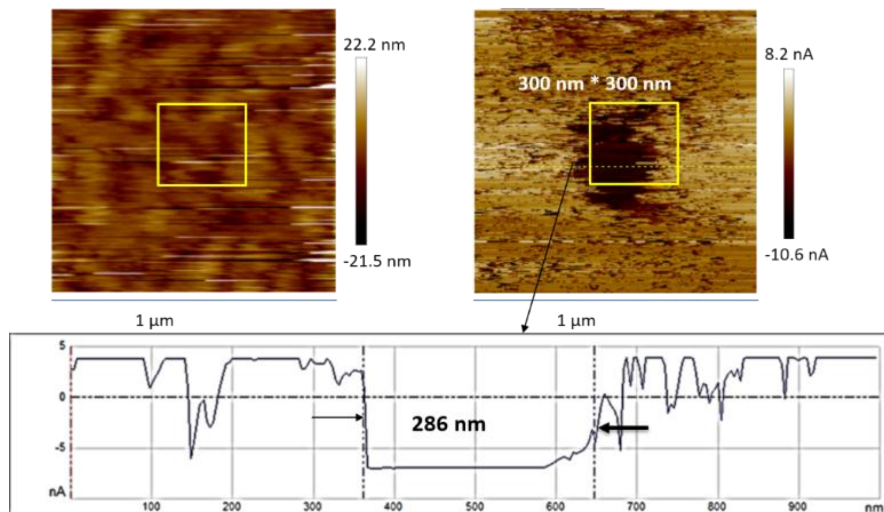

[b]. Step 2: Imaging in a 3 µm scan area with a biasing voltage of 1 V

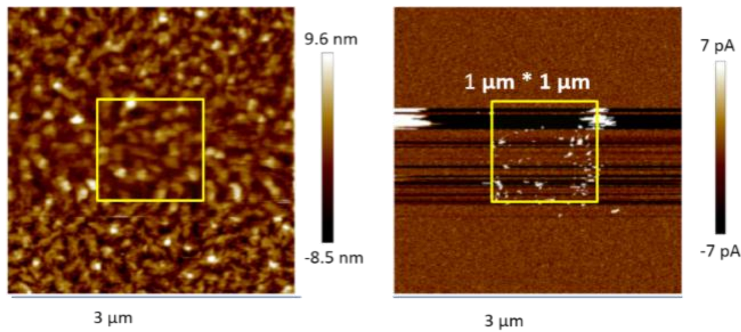

[c]. Step 3: Imaging in a 3 µm scan area with a biasing voltage of 3 V

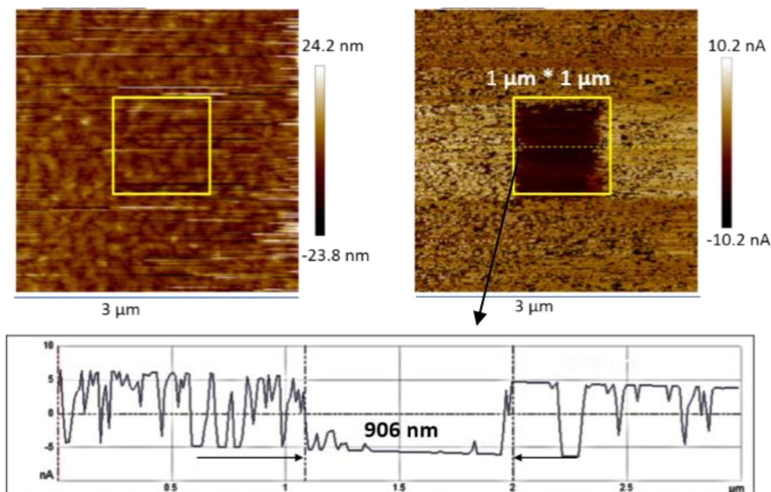

[d]. Step 4: Imaging in a 10 µm scan area with a biasing voltage of 1 V

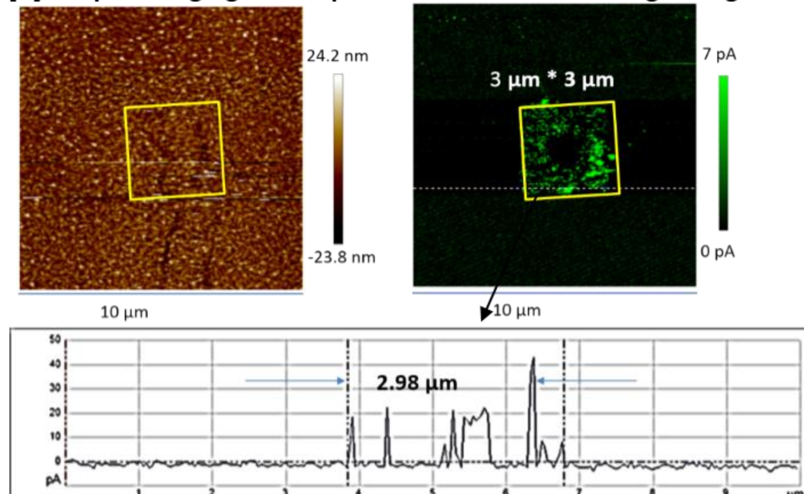

Fig 4.5.3.2: Steps [a], [b], [c] and [d] explain the sequence of C-AFM scans to realize the memory switching behavior.

After all we realized the 300 x 300 nm crystalline region in a 1 x 1 µm region, we scanned the same 1 x 1 µm region with a biasing voltage of 3 V to make the whole region

crystalline. We could observe that the earlier scanned 300 x 300 nm region was observed with negative current whereas the surrounding region was observed with positive current. From the line profile drawn for the current mapping image in the above figure 4.6.3.2 [a], it is clear that the earlier scanned and crystallized 300 x 300 nm region is showing a current contrast with a negative current with the surroundings. Such behavior was further confirmed by repeating the same set of experiments by scanning a 1 x 1 μm region and made crystalline. It was observed encompassed in a 3 x 3 μm region by applying possible read voltage of 1 V. But when the 3 x 3 μm region was scanned with high biasing voltage, it has shown the 1x1 μm crystallized region with the negative polarity as the way the 300 x 300 nm region was observed in a 1 x 1 μm region with high biasing voltage. The 3 x 3 μm crystallized region was again reproduced in a 10 μm region when we applied a low bias voltage of 1 V. The yellow boxes shown in the current mapping of 1 x 1 μm, 3 x 3 μm and 10 x 10 μm represent the crystallization suffered region in the previous scans to that particular scan. The negative polarity observed in memory switched could be due to the capacitive nature of the surface on subjecting to higher voltages. In addition it is also worth mentioning that GeTe in crystalline form is expected to exhibit ferroelectric character, hence, there is a possibility that the capacitive nature is enhanced in crystalline form and is discharging during the consecutive scan. However, the origin of such behavior remains ambiguous and further investigations are under progress.

4.5.4 Delay time dependence on switching behavior of amorphous thin films

We have investigated the delay time dependence on threshold switching behavior of amorphous thin films. The delay time dependence measurements were performed using C-AFM ramp mode operation. In the ramp mode, by setting different ramp rates, we can change the delay times. Restricted to the limitations of the AFM equipment, we could vary the delay time ranges from ~1 ms to ~100 ms corresponding to their ramp rates from 0.01 Hz to 1 Hz. The ramp voltage applied to investigate the delay time dependence is 0 to 3 V. In a single probe point, ramp voltage is applied with different ramp rates i.e. different delay times to investigate the delay time dependence on the threshold switching. The figure 4.5.4.1 gives the overall picture of the threshold switching voltages observed for I-V characteristics performed at different ramp rates.

Ramp rate	Total Ramp time (in Seconds)	Delay time b/ w the data points (in m.Sec)
0.01	100	100
0.02	50	50
0.03	33	33
0.04	25	25
0.05	20	20
0.06	16	16
0.08	12	12
0.1	10	10
0.2	5	5
0.3	3	3
0.4	2	2
0.5	2	2
0.6	1.6	1.6
0.8	1.2	1.2
1	1	1

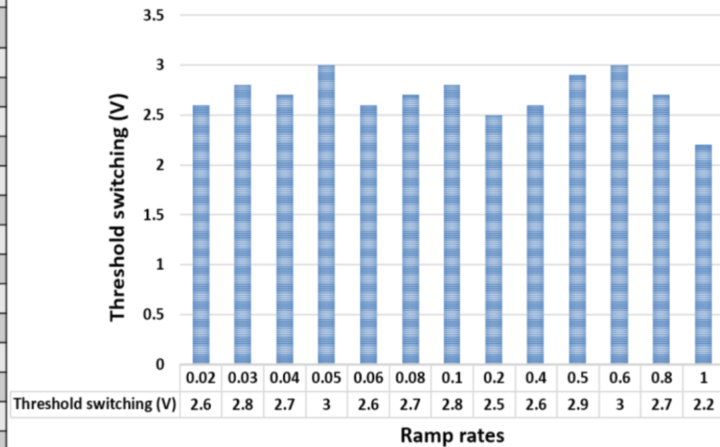

Fig 4.5.4.1: (Left) Table gives the possible ramp rates and their corresponding delay times variable with C-AFM. (Right) Threshold switching values obtained with different ramp rates applied.

From the above figure, it is apparently seen that the threshold switching values observed for different ramp rates or delay times are almost uniform with a small spread. The threshold switching values have a spread in the range between 2.5 V and 3 V. Since the delay times are ranging from 1 ms to 100 ms which are far higher than what the literature reported about the crystallization times (~100μs) for $Ge_{15}Te_{85}$ [11], the switching is predominant. No considerable delay time dependence on the threshold voltages was observed.

In summary, we were able to successfully obtain i) a switching characteristic at nanoscale with a very stable threshold voltage as compared to the bulk counterpart of same $Ge_{15}Te_{85}$ systems, ii) A nanoscale control over resistive switching and memory switching on a given region of $Ge_{15}Te_{85}$ thin films and iii) most importantly with a least dependence on delay times within the instrumental limit of variation in delay time

References

1. Hoyer, W., I. Kaban, P. Jóvári, and E. Dost. "Crystallization behavior and structure of amorphous Ge15Te85 and Ge20Te80 alloys." Journal of non-crystalline solids 338 (2004): 565-568.
2. Kolobov, A. V., J. Tominaga, P. Fons, and T. Uruga. "Local structure of crystallized GeTe films." Applied physics letters 82, no. 3 (2003): 382-384.

3. Jóvári, P., I. Kaban, W. Hoyer, R. G. Delaplane, and A. Wannberg. "Local atomic environment in amorphous Ge15Te85." Journal of Physics: Condensed Matter 17, no. 10 (2005): 1529..
4. Uemura, O., N. Hayasaka, S. Tokairin, and T. Usuki. "Local atomic arrangement in Ge-Te and Ge-S-Te glasses." Journal of non-crystalline solids 205 (1996): 189-193.
5. Kaban, I., Th Halm, W. Hoyer, P. Jóvári, and J. Neuefeind. "Short-range order in amorphous germanium–tellurium alloys." Journal of non-crystalline solids 326 (2003): 120-124.
6. Zoski, Cynthia G. Handbook of electrochemistry. Elsevier Science Limited, 2007.
7. Banerjee, S., M. Sardar, N. Gayathri, A. K. Tyagi, and Baldev Raj. "Conductivity landscape of highly oriented pyrolytic graphite surfaces containing ribbons and edges." Physical Review B 72, no. 7 (2005): 075418.
8. Adler, David, Heinz K. Henisch, and Sir Nevill Mott. "The mechanism of threshold switching in amorphous alloys." Reviews of Modern Physics 50 (1978): 209-220.
9. Fritzsche, Hellmut. "Why are chalcogenide glasses the materials of choice for Ovonic switching devices?." Journal of Physics and chemistry of Solids 68, no. 5 (2007): 878-882.
10. Nevill, Mott. "Conduction in amorphous materials." Electronics & Power 19, no. 14 (1973): 321-324.
11. Chen, M., K. A. Rubin, and R. W. Barton. "Compound materials for reversible, phase-change optical data storage." Applied physics letters 49, no. 9 (1986): 502-504.

Chapter 5

Summary and Conclusions

In the present investigation, an attempt has been made to understand the nanoscale electrical characterization of $Ge_{15}Te_{85}$ thin films using C-AFM. The writing and reading operations at nanoscale regions were performed using C-AFM tip. The two important effects that are associated with the phase change materials (threshold switching and memory switching) were studied.

1. As-deposited thin films obtained were characterized using SEM-EDS to analyze the composition and it was found that the composition of the sputtered thin films was $Ge_{15}Te_{85}$ ($GeTe_6$) and also homogeneity of the composition was confirmed over a region of 15 mm x 15mm.
2. From the structural characterization by X-ray diffraction, we confirm that the as-deposited thin films are in amorphous state.
3. The room temperature Raman scattering studies performed on $Ge_{15}Te_{85}$ thin films proved that there were no Ge-Ge bonds and the modes of Ge-Te (127 cm^{-1}) and a stronger overlapping of Ge-Te and Te-Te (143 cm^{-1}) bonds were present as observed for a Te-rich GeTe system.
4. The AFM studies of surface morphology makes clear that the surface of the thin films is so smooth, showing an rms roughness ranges from 1 nm to 2 nm.
5. The C-AFM operation on amorphous thin films exhibited both the resistive and memory switching effects. Observed threshold switching voltages by performing I-V ramps in different regions were in the range of 2 V to 3 V.
6. Overall the behavior of various I-V ramps performed in different regions exhibited consistent switching characteristics (both resistive and memory switching). The

variation in holding voltage observed is thought to be because of the voltage drop associated with different probe points.

The delay time dependence observed on threshold switching values is found to be negligible. The delay times ranging from 1 ms to 100 ms, were utilized and no appreciable change in threshold switching was observed.

However, the memory switching characteristics was also confirmed by performing scans at different regions under different bias conditions. A region with smaller scan area, say 300 x 300 nm was memory switched by performing a scan with a bias voltage of 3V. The consecutive scan of larger area say 1 x 1 μm encompassing the previous 300x300nm scan clearly revealed that the earlier scanned region has undergone a complete amorphous to crystalline transformation. Such a transformation was confirmed by the high conducting state of current map image obtained from C-AFM. Thus the memory switched regions with the use of large biasing voltages were reproduced by applying sufficiently low biasing voltages (read voltages) and confirmed from the electrical contrast observed for memory switched region. Similar studies were performed at different regions with different scanning areas and bias voltages. It is evident that $Ge_{15}Te_{85}$ thin films undergo memory switching associated with amorphous to crystalline transformation and most importantly, such a transformation could be controlled externally at nanoscale utilizing C-AFM.

The major problem of phase segregation of Te though is not observed with the electric field induced crystallization. But, the memory switching and threshold switching behavior of $GeTe_6$ thin films was observed at low voltages ($\leq$ 3 V). There were few practical difficulties, such as varying the delay times less than 1 ms and scanning in areas less than 300 nm, which are associated with the scanner configuration. Because of high delay times and small range of biasing voltage featured with the available scanner, it was not possible for us to erase a memory switched region. It was also difficult to study the ovonic threshold switching behavior, since the switching characteristics drastically change with increase in delay times. Specifically, the delay times we employed to study the switching behavior are most favorable for memory switching. We have tried to reproduce the memory switched region with possible low voltage values ($\leq$ 1.5 V).

Future work

Though $Ge_{15}Te_{85}$ as a phase change memory failed to attract the technological applications, but the faster ovonic threshold switching characteristics of $Ge_{15}Te_{85}$ are so advantageous to be used as an OTS selector device. A rightly prepared sample could throw more light on the electrical characterization at nanoscale and understanding the phase separation involved in eutectic materials. Thermal annealing treatments with different temperatures could also be performed to analyze the problem of phase separation under scanning probe studies.